J. Fluid Mech. (1972), *vol.* 56, *part* 3, *pp.* 447–479
Printed in Great Britain

Experiment on the geometry of the fine-structure regions in fully turbulent fluid

By ALBERT YI-SHUONG KUO† AND STANLEY CORRSIN
Department of Mechanics, The Johns Hopkins University

(Received 10 May 1972)

An attempt has been made to identify the geometric character of the random fine-structure regions dispersed in fully turbulent fluid. The technique was measurement of two-position coincidence functions for the presence of velocity fine-structure. In this primitive approach, we tried to distinguish among only three possible categories for the random shapes: (*a*) 'blobs', (*b*) 'rods' and (*c*) 'slabs', depending on whether three mean orthogonal dimensions of the domains were such that (*a*) all were of the same order, (*b*) one was an order larger than the other two, or (*c*) one was an order smaller than the other two.

Highly idealized paradigms for these three categories were studied analytically: the two-position coincidence functions were computed for the cases of (*a*) spheres, (*b*) circular cylinders and (*c*) plane slabs, each field containing randomly sized elements distributed randomly in space with a homogeneous and isotropic distribution. Comparison of the measured coincidence functions with these three paradigms suggests that the fine-structure regions are more nearly of 'rod-like' geometry than like either of the other two. No attempt was made to distinguish shapes which might be called 'strips'.

1. Introduction

It has been found (e.g. Batchelor & Townsend 1949; Kuo & Corrsin 1971, referred to in this paper as I) that in fully developed turbulent flow, especially at large Reynolds numbers, the fine-scale motion is localized in relatively small regions which are distributed randomly throughout the flow field. Since the viscous dissipation of turbulent kinetic energy occurs primarily in the fine-structure ('small eddies'), this implies that the dissipation regions may be scattered throughout the fluid in a rather 'spotty' way.

Townsend (1951*a*) suggested that the smallest scale components (smaller than the Kolmogorov microscale) can be modelled as sheets or lines of vorticity passively superimposed on the main turbulence field. These sheets or lines presumably reach a transient quasi-equilibrium condition in which the gain of 'energy' from distortion is balanced by viscous diffusion and dissipation. He

† Present address: Virginia Institute of Marine Science, Gloucester Point, Virginia 23062.

computed the spectral forms which would be produced by random distributions of vortex 'sheets' and by random distributions of vortex 'lines'. Better agreement with experiment was obtained from his vortex-sheet model. Batchelor (1959) raised some doubts about Townsend's analysis of these models, after doing a similar analysis on turbulent mixing of scalar fields with very large Prandtl (or Schmidt) number. These analyses were not concerned with spottiness; they assume in effect that the fine-structure is homogeneously distributed in space in any one realization.

Some years later, Corrsin (1962) devised a very explicit 'spotty' model, with energy dissipation localized in randomly distributed thin sheets (or slabs). He assumed a slab thickness of the order of the Kolmogorov microscale and spacing of the order of the integral scale. His model estimates that the flatness factor of the first derivative of velocity fluctuations increases as $R_\lambda^{\frac{3}{2}}$, where R_λ is the Reynolds number. Tennekes (1968) modified this by suggesting a model of randomly distributed 'vortex tubes', with diameters of the order of the Taylor microscale λ. This gives a flatness factor increasing linearly with R_λ. In I the estimated empirical result is that the flatness factor $\sim R_\lambda^{0.6}$ for large R_λ.

Up to now no experiment has been performed to evaluate these models directly or, in fact, to assess the geometry explicitly. The present investigation is an experimental attempt at categorizing the random geometry of the small regions in which the fine-scale structure is active. Such information may eventually help an understanding of the physical process of turbulent energy transfer across the wavenumber spectrum, from spatially more evenly distributed large scales to unevenly distributed fine scales.

The topics in this paper are presented in the following order.

(*a*) Equipment and experimental procedure (§2).

(*b*) Preliminary discussion of the three idealized geometric models which will be used to interpret the data.

(*c*) Mathematical analysis of the *single-probe* signal statistics which would occur for each of the three geometric models (§3.1).

(*d*) Mathematical analysis of the *two-probe* signal statistics which would occur for each of the three geometric models (§3.2).

(*e*) The actual single-probe and two-probe data (§4) and the comparisons with (*c*) and (*d*), to decide which of the three geometric models comes closest to the actual data (§§4 and 5).

2. Experimental equipment and procedure

The flow field is a grid-generated turbulence homogeneously strained by a slight contraction to bring it close to isotropy (see Comte-Bellot & Corrsin 1966). The wind tunnel has a closed circuit and a test section 32 ft long and 3×4 ft in cross-section. The grid is of square rod, square mesh, biplane construction. The grid mesh size is 4 in. and the mean velocity in the test section is 12·7 m/s. Measurements were made 42 mesh lengths downstream from the grid, where the turbulent field has been found to be more or less isotropic, with $R_\lambda = 110$. The measured one-dimensional spectrum function of u_1 is shown in figure 1.

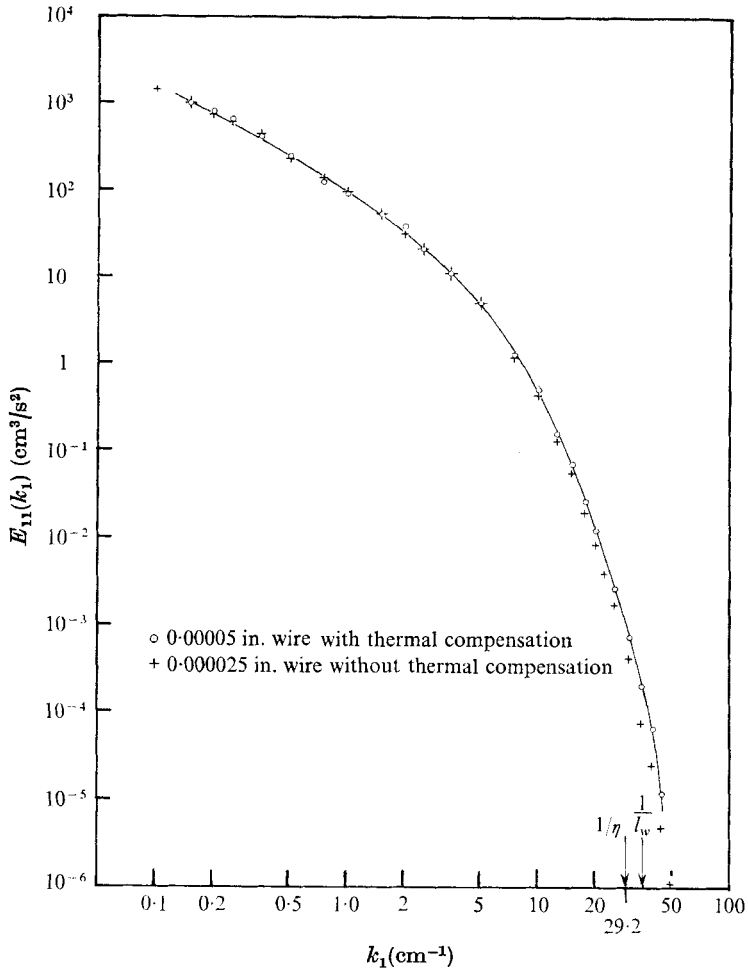

FIGURE 1. One-dimensional energy spectrum $E_{11}(k_1)$ in the (grid-generated isotropic) turbulence. Downstream distance $x_1/\eta = 43$; $R_\lambda = 110$. k_1 is the wavenumber, $u_1' = 23{\cdot}1$ cm/s is the root-mean-square turbulent velocity component, η is the Kolmogorov micro-scale, l_w is hot-wire length. The data were not corrected for finite length of wire. $\bar{U} = 12{\cdot}7$ m/s; integral scale = 5·04 cm.

The component energy decays are presented by Comte-Bellot & Corrsin (1966). Details of measuring devices are given in I.

Velocity fluctuations were measured with Shapiro & Edwards constant-current hot-wire anemometer units. Hot-wire probes were made of jeweller's broaches encased in Nu-Weld dental cement, with $\frac{1}{4}$ in. stainless-steel tubes as main shafts. For two-probe measurements, one was bent up at an angle (see figure 2) to minimize interference and to allow 'meshing' of the two probes to aid in determining zero separation. The separation distances r_1 and r_2 were controlled by and read on micrometers graduated in thousandths of an inch.

Only the streamwise turbulent velocity component u_1 was measured, with a single wire set normal to the mean flow. All data were taken with platinum–(10 %) rhodium wire etched from Wollaston type after the silver coating had

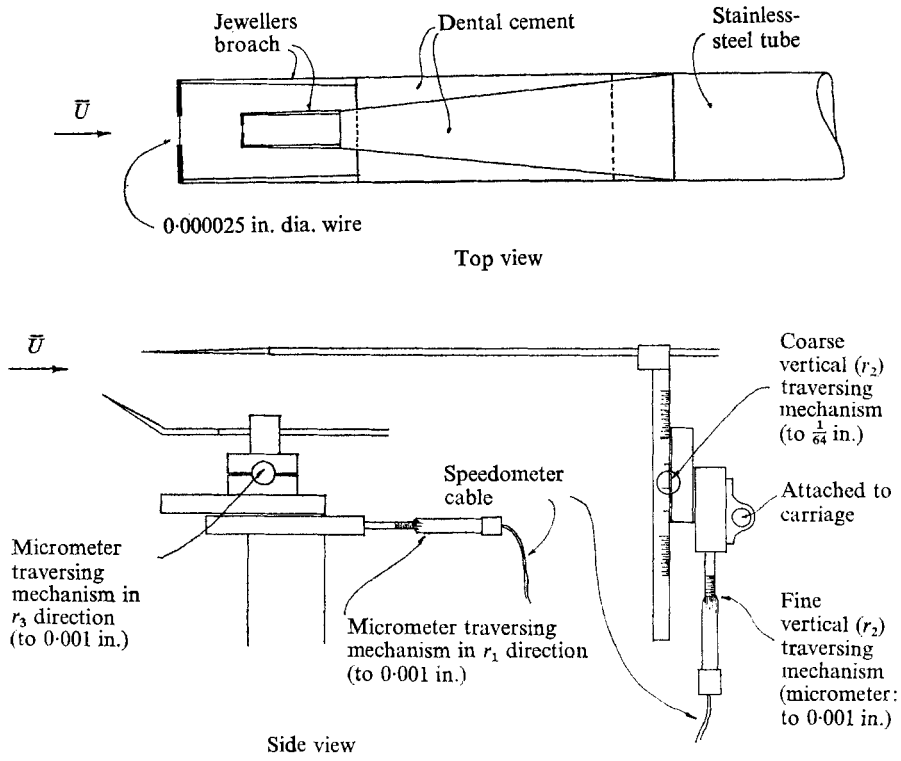

FIGURE 2. Sketch of hot-wire probe configuration and traversing mechanism.

been soldered to the tips of the jeweller's broaches. In order to increase the signal-to-noise ratio, 0·000025 in. wires, 0·01 in. long, were used without thermal compensation. The reciprocal of the thermal time constant of this wire is about 6·5 kHz, which is higher than the Kolmogorov-scale frequency (5·9 kHz) of the turbulent flow, i.e. the frequency generated at the probe when a disturbance of size equal to the Kolmogorov microscale $\eta \equiv (\nu^3/\langle\epsilon\rangle)^{\frac{1}{4}}$ is convected past by the mean flow $\bar{U}$.

To be able to infer the geometry of the fine-structure regions, first a choice of fine-structure signal must be made. A signal which is easy to obtain and has obvious physical meaning is the time derivative of the velocity fluctuations, which is related to the strain rate and energy dissipation. Unfortunately, a turbulent flow field with Reynolds number high enough to 'decouple' the dissipation spectrum from the energy spectrum is not easy to obtain in the laboratory. Therefore, in this investigation, four-pole Butterworth high-pass filters were used to extract 'fine-structure signals'. The filters have a sharp enough low frequency cut-off (24 db/octave) to eliminate the large-scale signals from the output (see I).

The fine-structure signal $e(t)$ from the output of the Butterworth filter appeared intermittent. The technique used to exploit this intermittent signal involves generating a signal $I(t)$, which is a random square wave, equal to a non-zero constant (e.g. 1·0) when $e(t)$ is at its 'higher state' and zero when $e(t)$ is at its

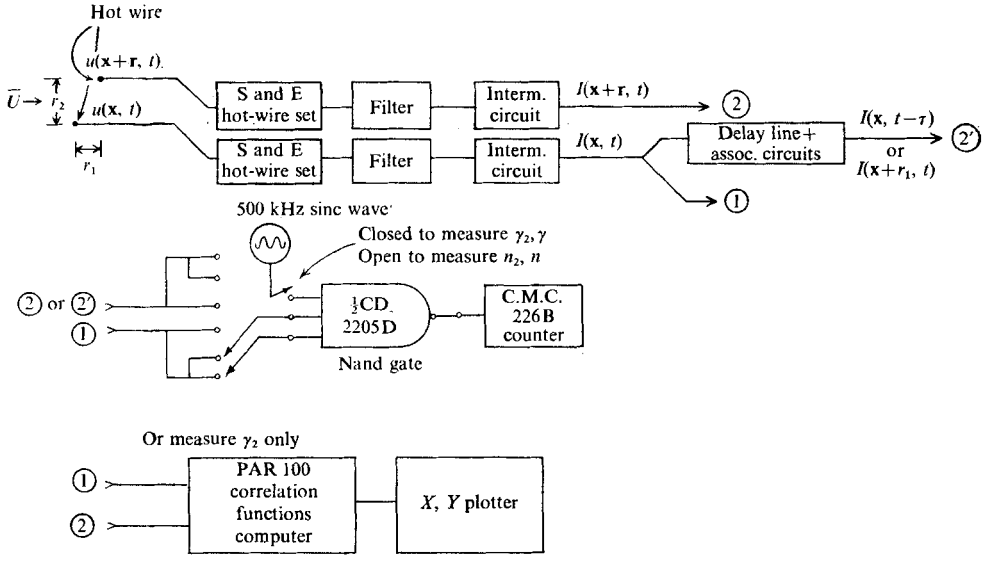

FIGURE 3. Block diagram of circuit arrangements for measuring n_2 and γ_2.

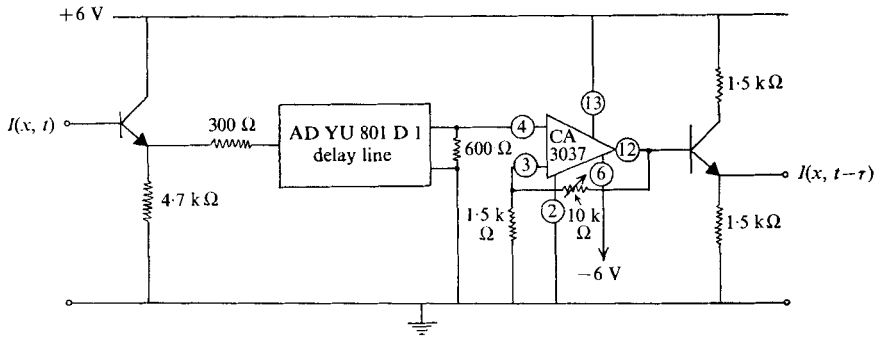

FIGURE 4. Circuitry associated with delay line.

'lower state'. $I(t)$ then tells us when the hot wire is in a fine-structure region and when it is not. Two properties of $I(t)$ were measured, the average pulse frequency n and the 'intermittency factor' γ. The electronic circuits used to generate $I(t)$ and those used to measure n and γ are described in I.

To avoid wake interference effects in determining the coincidence function with one sample point directly downwind of the other, we used a single probe for this case, measuring the 'auto-coincidence' function. Here we used the 'Taylor approximation', which equates time dependence at a fixed point in the flow to space dependence along the mean flow direction. It has been shown by Comte-Bellot & Corrsin (1971) that this is a good approximation for a small turbulence level flow much like that studied here.

Figure 3 shows the block diagram of the instruments used to measure the probability that two hot wires are in fine-scale-structure regions simultaneously. An ADYU Model 801D1 delay line was used, when appropriate, to delay the signal from a single hot wire. In order to match the impedances of the delay line

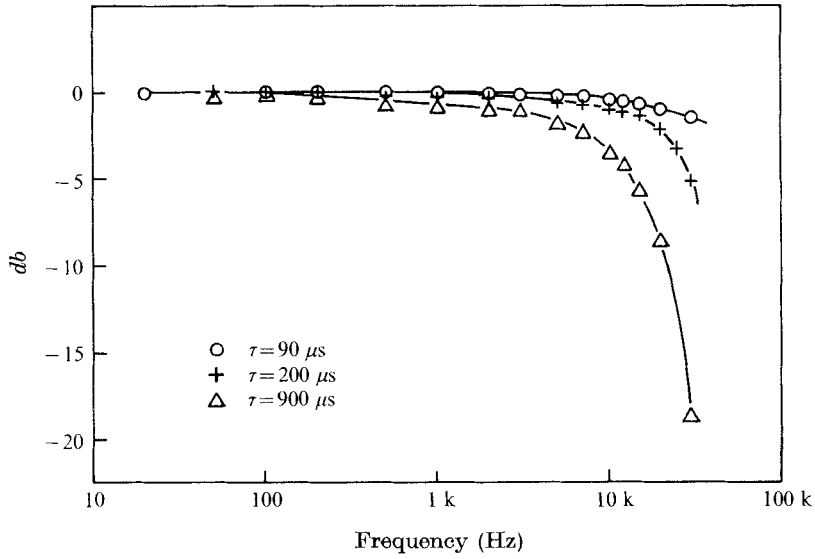

FIGURE 5. Frequency response of delay line. τ is delay time.

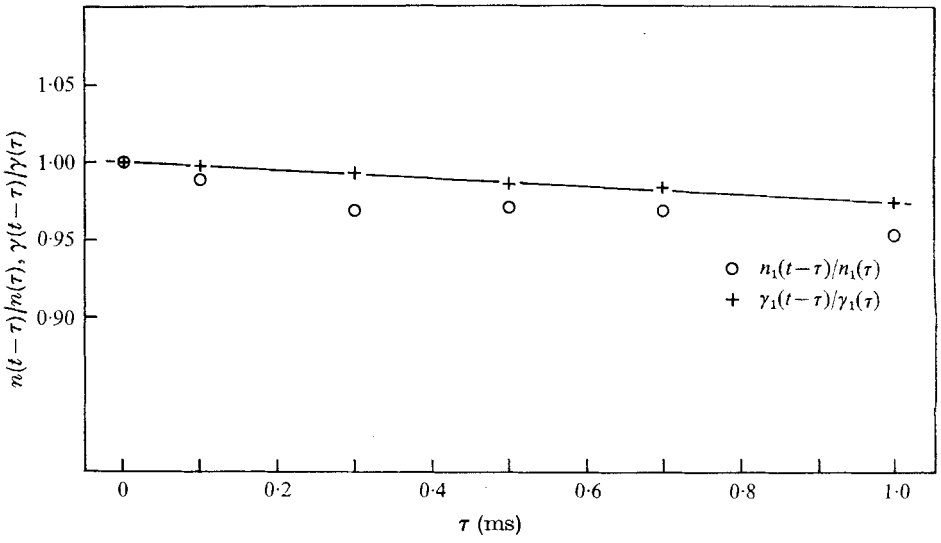

FIGURE 6. Performance check of full delay circuitry.

and regain the attenuation through it, operational amplifier and emitter followers were used in conjunction with it as shown in figure 4. The frequency response of the delay line circuit is shown in figure 5. A performance check of the delay line was made by comparing the pulse frequencies and the intermittency factors of the random square waves at the input and output of the circuit. Figure 6 shows that these values are quite close to unity, so wave form reshaping was not necessary.

Two statistical properties of coincidence were measured: the average frequency of occurrence of coincidence, n_2, and the relative time fraction during which

coincidence existed, γ_2. The 'coincidence' referred to is the simultaneous immersion of both probes in turbulent fine-structure. They were measured in the same ways as n and γ. In cases when one of the $I(t)$ signals was to be delayed, γ_2 was measured more conveniently with a PAR Model 100 correlation function computer. The computer calculates the cross-correlation of its inputs; an X, Y plotter can record the cross-correlation as a function of the delay time τ. The cross-correlation coefficient is just the ratio of γ_2 to γ.

3. Analysis of geometric models

The experimental evidence showed that at large enough Reynolds numbers the fine-scale components of turbulence are localized in relatively small regions of the fluid. These small regions are presumably convected and strained by the larger scale turbulence.

Let us consider a fluid element small enough that the instantaneous strain rate is approximately uniform over it. If the strain-rate tensor of the fluid element is described in principal-axis co-ordinates, it takes the form

$$\begin{Bmatrix} S_1 & 0 & 0 \\ 0 & S_2 & 0 \\ 0 & 0 & S_3 \end{Bmatrix},$$

where S_1, S_2 and S_3 are the principal rates of strain. In an incompressible turbulent fluid, S_1, S_2 and S_3 are random variables satisfying the (mass balance) condition

$$S_1 + S_2 + S_3 = 0.$$

Therefore, S_1, S_2 and S_3 cannot all be of the same sign simultaneously. If the rotation of the principal axes relative to the fluid element is small enough during a time interval comparable to the Kolmogorov time scale

$$[t_K = (\nu/\langle\epsilon\rangle)^{\frac{1}{2}} \approx (\text{r.m.s. vorticity})^{-1}]$$

of the turbulence, the Lagrangian time averages $\tilde{S}_1, \tilde{S}_2$ and $\tilde{S}_3$ may be taken as the average strain rates in fixed directions relative to the fluid material element.† At the end of a time interval t_K, a fluid element with three orthogonal dimensions of the same order of magnitude initially will have one of the following shapes, according to the signs of $\tilde{S}_1, \tilde{S}_2$ and $\tilde{S}_3$:

(*a*) $l_1 \approx l_2 \approx l_3$, if $\tilde{S}_1 \approx \tilde{S}_2 \approx \tilde{S}_3 \approx 0$;

(*b*) $l_1 \approx l_2 < l_3$, if $\tilde{S}_1 \approx \tilde{S}_2 < 0$, $\tilde{S}_3 > 0$;

† Rigorous proof of the persistence of the local straining motion has not yet been obtained. There are some grounds for belief that the direction of the principal axes relative to the fluid element changes relatively slowly. The degree of persistence of local straining motion, particularly the principal rate of strain and the direction of the principal axes, has been discussed by Batchelor (1959) and Batchelor & Townsend (1956). Some evidence of the persistence of any type of strain referred to axes rotating with the fluid element was demonstrated by Townsend (1951*b*) in measurements of cooling of heat spots in a turbulent fluid. More recent relevant discussion can be found in a paper of Lumley (1972).

(*c*) $l_1 < l_2 \approx l_3$, if $\tilde{S}_1 < 0$, $\tilde{S}_2 \approx \tilde{S}_3 > 0$;

(*d*) $l_1 < l_2 < l_3$, if $\begin{cases} \tilde{S}_1 < 0, & \tilde{S}_3 > \tilde{S}_2 > 0 \\ \text{or} & \tilde{S}_1 < \tilde{S}_2 < 0, \quad \tilde{S}_3 > 0; \end{cases}$

where l_1, l_2 and l_3 are three orthogonal 'principal' dimensions of the fluid element after being strained.

Since t_K^{-1} is of the same order of magnitude as the strain rates, t_K is not a long enough time for strong inequalities between the l's to develop. Yet the tendencies presumably persist for times larger than t_K, so we may expect (with distortion) for larger times one of the following.

(*a*) A 'blob': $l_1 \approx l_2 \approx l_3$, if $\tilde{S}_1 \approx \tilde{S}_2 \approx \tilde{S}_3 \approx 0$.

(*b*) A 'rod': $l_1 \approx l_2 \ll l_3$, if $\tilde{S}_1 \approx \tilde{S}_2 < 0$, $\tilde{S}_3 > 0$.

(*c*) A 'slab': $l_1 \ll l_2 \approx l_3$, if $\tilde{S}_1 < 0$, $\tilde{S}_2 \approx \tilde{S}_3 > 0$.

(*d*) A 'ribbon': $l_1 \ll l_2 \ll l_3$, if $\begin{cases} \tilde{S}_1 < 0, & \tilde{S}_3 > \tilde{S}_2 > 0 \\ \text{or} & \tilde{S}_1 < \tilde{S}_2 < 0, \quad \tilde{S}_3 > 0. \end{cases}$

The above four possible categories of geometry are the result of the straining of an initially 'blob-like' geometry. Since the detailed process of the generation of the fine-structure from the large-scale motions is pretty well unknown, we have looked simply at an initially 'blob-like' geometry having no initial preferred direction. The above categories include all possible classes of relationships among the relative magnitudes of the l's.

For simplicity in this preliminary investigation, we make no attempt to distinguish case (*d*). The first alternative in (*d*) is vaguely related to (*c*), while the other is vaguely related to (*b*). Therefore only three possible categories of geometries will be analysed and identified in this paper.

In order to establish distinct differences in measurable statistical functions for the three geometric categories, we now analyse three special kinds of random binary fields which may be considered as paradigms for the three categories: spheres as model 'blobs', infinite circular cylinders as model 'rods' and infinite plane slabs as model 'slabs'. We consider (*a*) spheres, randomly positioned and with random diameters l, or (*b*) infinitely long circular cylinders, randomly positioned, randomly and isotropically oriented, and with random diameters l, or (*c*) infinite plane slabs, randomly positioned, randomly and isotropically oriented and with random thickness l. l is a random variable with probability function $g(l)$ defined as follows.

(*a*) *Sphere model.* $g(l)\,dl$ is the average number of spheres per unit volume of space with diameters between l and $l+dl$, so the average number of spheres in a unit volume is

$$N = \int_0^\infty g\,dl,$$

if the density of spheres is so small that the overlap is negligble.

(*b*) *Cylinder model.* $g(l)\,dl$ is the average length of cylinders per unit volume of

space with diameters between l and $l+dl$, so the average total length of cylinders in unit volume is

$$L = \int_0^\infty g\,dl,$$

if the density of cylinders is so small that the overlap is negligible.

(*c*) *Slab model.* $g(l)\,dl$ is the centre-plane area per unit volume of space of slabs with thicknesses between l and $l+dl$, so that the average total area of slabs in unit volume is

$$S = \int_0^\infty g\,dl,$$

if the density of slabs is so small that the overlap is negligible.

3.1. *Single-probe detection*

As the fine-structure active regions are swept past by the mean flow, the hot wire and the associated electronic circuits put out a random square-wave signal $I(t)$, with level 1·0 at times when the hot wire is in a fine-structure region and level 0 at other times. Two independent statistical quantities obtainable from $I(t)$ are the intermittency factor γ, the fraction of time during which $I(t)$ is at the level 1·0, and n, the average number of 'pulses' per unit time.

It can easily be shown that the intermittency factor γ equals γ_s, *the fractional volume of space occupied by the fine-structure.* If a straight line is drawn through the flow field at any instant, the length fraction that lies within fine-structure regions is γ_s, since for each point on the line the probability that it lies inside the regions is γ_s. The quantity γ of $I(t)$ corresponds to what would be obtained by drawing a sampling line in the mean flow direction, if the 'Taylor approximation'† holds true.

γ and n may also be computed for the three paradigms listed above. Let $m = n/U$, the average number of the fine-structure regions 'detected by the hot wire' per unit distance it traverses, and $\langle w\rangle = \gamma/m$, the average dimension of the fine-structure regions as 'measured by the hot wire'. In all of the following analysis, consider these fine-structure regions to be in a cube of unit volume with one side parallel to the mean flow. As the cube is convected by the mean flow past the hot wire, the 'expected' number of the fine-structure regions detected is m and the sum of the linear dimensions w of these detected regions is γ, when length is measured in the same units as the 'unit' cube. The co-ordinate system is chosen so that the hot wire is at the origin and the mean flow is in the positive-x direction.

(i) *Sphere model.* The probability that a sphere in the unit cube is detected by a point probe is the ratio of its projected area to the projected area of the unit cube on the y,z plane, i.e. $\frac{1}{4}\pi l^2$/unit area $= \frac{1}{4}\pi l^2$. The expected number of spheres with diameters between l and $l+dl$ detected during the time when the unit cube is swept past the probe is

$$g(l) \times \tfrac{1}{4}\pi l^2\,dl. \tag{3.1}$$

Therefore,

$$m = \tfrac{1}{4}\pi \int_0^\infty l^2 g(l)\,dl, \tag{3.2}$$

i.e.

$$m = \tfrac{1}{4}\pi N\langle l^2\rangle,$$

† See appendix.

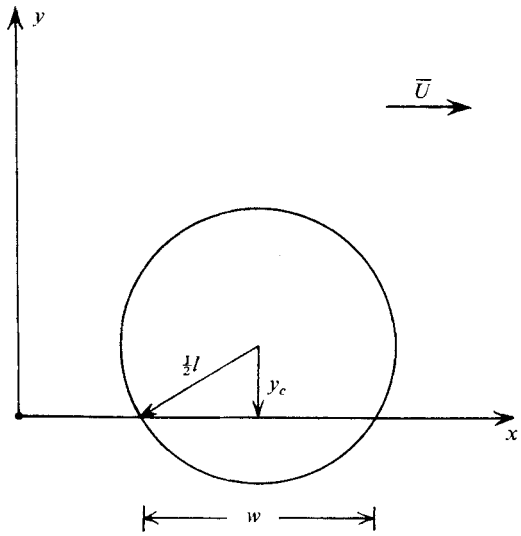

FIGURE 7. Geometry for single-probe detection of a sphere convected in the x direction.

where $\langle\ \rangle$ means expectation value (i.e. ensemble average). In deducing (3.2) we have ignored spheres which lie partly outside the cube because we can choose this 'unit cube' as large as we like, so large in fact that such 'boundary effects' are negligible.

To compute $\langle w \rangle$ as a function of $g(l)$, we consider a sphere carried along by the mean flow with its centre off the x axis. We rotate our co-ordinates about the x axis until the x, y plane passes through the sphere centre, so that the 'radial' distance from the x axis to the sphere centre is y_c, as shown in figure 7. Then the point probe will measure the following value of w as the sphere passes:

$$w = \begin{cases} 2[(\frac{1}{2}l)^2 - y_c^2]^{\frac{1}{2}} & \text{if} \quad y_c \leqslant \frac{1}{2}l, \\ 0 & \text{if} \quad y_c \geqslant \frac{1}{2}l. \end{cases}$$

The average number of spheres with diameters between l and $l+dl$ detected by the probe is given by equation (3.1). Among these spheres, the probability that a centre lies in the differential annulus $y_c \leqslant y \leqslant y_c + dy_c$ around the x axis is $2\pi y_c dy_c / \frac{1}{4}\pi l^2$. Therefore, the intermittency factor seen by the probe is

$$\gamma = \int_0^\infty \int_0^{\frac{1}{2}l} 2[(\tfrac{1}{2}l)^2 - y_c^2]^{\frac{1}{2}} \left(\frac{2\pi y_c}{\frac{1}{4}\pi l^2}\right) g(l)\,(\tfrac{1}{4}\pi l^2)\, dy_c\, dl,$$

which turns out to be

$$\gamma = \tfrac{1}{6}\pi N \langle l^3 \rangle, \tag{3.3}$$

which is the expected total volume in spheres of all sizes, per unit volume of space. From (3.2) and (3.3),

$$\langle w \rangle = \gamma / m = \tfrac{2}{3}\langle l^3 \rangle / \langle l^2 \rangle; \tag{3.4}$$

N has cancelled out.

† The upper limit of ∞ for integration over l is permitted in spite of the fact that the analysis is over spheres fully contained in a 'limit cube', because the unit cube can be as large as we like.

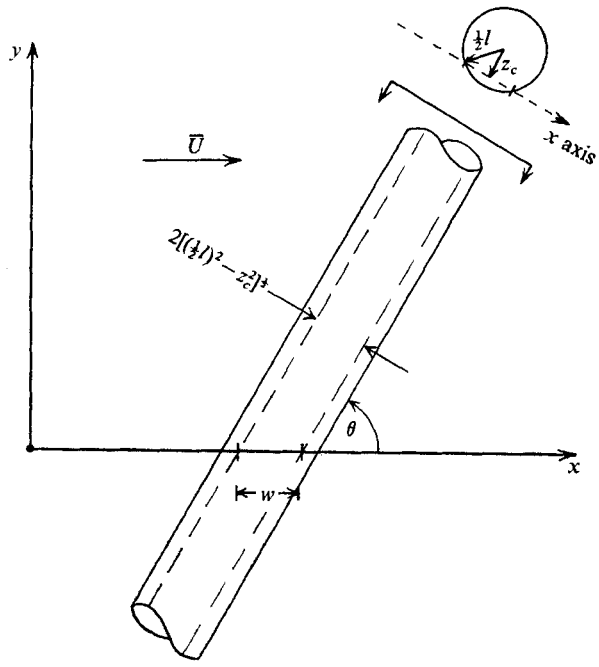

FIGURE 8. Geometry for single-probe detection of a cylinder convected in the x direction.

(ii) *Cylinder model.* The probability that any unit length of cylinder is detected by a point probe equals the ratio of its projected area to the projected area of the unit cube on the y, z plane, i.e.

$$l \sin\theta \times \text{unit length/unit area} = l \sin\theta,$$

where θ is the angle between the cylinder axis and the x axis. Since the orientation of cylinders is statistically isotropic, the probability density of θ is the measure of relative solid angle corresponding to θ, i.e.

$$p_\theta(\theta) = \begin{cases} \sin\theta & \text{for} \quad 0 \leqslant |\theta| \leqslant \frac{1}{2}\pi, \\ 0 & \text{otherwise.} \end{cases}$$

The expected number of cylinders 'hitting' the probe and having diameters between l and $l+dl$ with orientation angles between θ and $\theta+d\theta$ is then

$$g(l) l \sin^2\theta \, d\theta \, dl \qquad (3.5)\dagger$$

for $0 \leqslant \theta \leqslant \frac{1}{2}\pi$ and $0 \leqslant l \leqslant \infty$. Therefore, the expected number of encounters is

$$m = \int_0^\infty \int_0^{\frac{1}{2}\pi} g(l) l \sin^2\theta \, d\theta \, dl,$$

i.e.

$$m = \tfrac{1}{4}\pi L \langle l \rangle. \qquad (3.6)$$

† We need not include the fact that for each (infinitely long) cylinder the actual axis length of each cylinder contained within the cube depends on location and orientation, because the 'unit cube' is allowed to be indefinitely large.

Figure 8 shows a cylinder being convected along the x axis with its axis at an angle θ to the x axis. The y axis is chosen so that the x, y plane is parallel to the cylinder axis, and the distance between them is called z_c. The probe will measure w as a dimension of the cylinder:

$$w = \begin{cases} (2/\sin\theta)\,[(\frac{1}{2}l)^2 - z_c^2]^{\frac{1}{2}} & \text{if} \quad |z_c| \leqslant \frac{1}{2}l, \\ 0 & \text{if} \quad |z_c| \geqslant \frac{1}{2}l. \end{cases}$$

Among those cylinders given by (3.5), the probability of one having its axis at a distance between z_c and $z_c + dz_c$ form the x, y plane is dz_c/l. Therefore, the intermittency factor is

$$\gamma = \int_0^\infty \int_0^{\frac{1}{2}\pi} \int_{-\frac{1}{2}l}^{\frac{1}{2}l} \frac{2}{\sin\theta}\,[(\tfrac{1}{2}l)^2 - z_c^2]^{\frac{1}{2}} g(l) \sin^2\theta \, dz_c \, d\theta \, dl,$$

which gives

$$\gamma = \tfrac{1}{4}\pi L \langle l^2 \rangle, \tag{3.7}$$

the average volume of the cylinders per unit volume of space.

From (3.6) and (3.7),

$$\langle w \rangle = \langle l^2 \rangle / \langle l \rangle; \tag{3.8}$$

L has cancelled out.

(iii) *Slab model.* The probability that any unit area of a thin slab is detected by a point probe equals the ratio of its projected area to the projected area of the unit cube, both on the y, z plane. This is just $\cos\theta$, where θ is the angle between a normal to the surface and the x axis. Since the distribution of slabs is statistically homogeneous and isotropic, the probability density of θ is the measure of relative solid angle corresponding to θ, i.e.

$$p_\theta(\theta) = \begin{cases} \sin\theta & \text{for} \quad 0 \leqslant \theta \leqslant \frac{1}{2}\pi, \\ 0 & \text{otherwise.} \end{cases}$$

The expected number of slabs 'hitting' the probe and having thickness between l and $l + dl$, with orientation angle between θ and $\theta + d\theta$ is then

$$\sin\theta \cos\theta \, g(l) \, d\theta \, dl \tag{3.9}$$

for $0 \leqslant \theta \leqslant \frac{1}{2}\pi$, $0 \leqslant l \leqslant \infty$. Therefore, the average number of events per unit distance is

$$m = \int_0^\infty \int_0^{\frac{1}{2}\pi} \sin\theta \cos\theta \, g(l) \, d\theta \, dl,$$

which gives

$$m = \tfrac{1}{2}S, \tag{3.10}$$

which is a particular application of a theorem of Corrsin (Corrsin 1955; Corrsin & Phillips 1961; Pawula 1968). In fact, (3.2) and (3.6) can also be obtained by applying that theorem to the randomly distributed spherical and cylindrical surfaces.

Figure 9 shows a plane slab being convected along the x axis with its normal at angle θ to the x axis. The y axis is chosen so that the x, y plane is normal to the slab surface. The probe will intercept the slab to give w as shown:

$$w = l/\cos\theta.$$

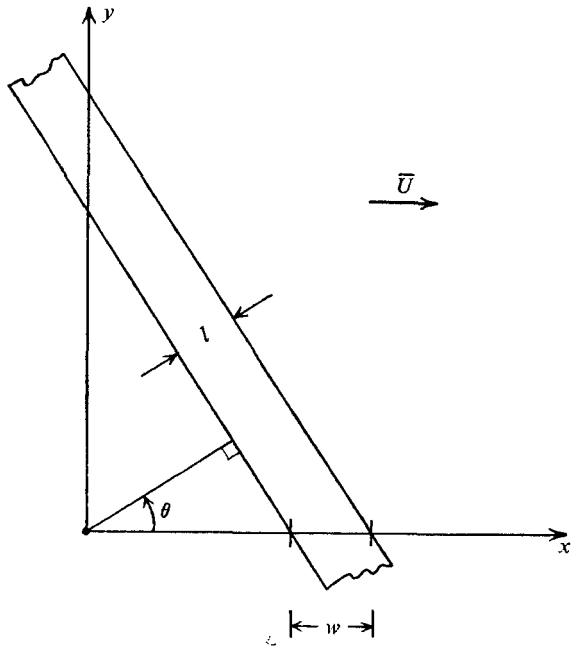

FIGURE 9. Geometry for single-probe detection of a slab convected in the x direction.

Combining with (3.9) gives

$$\gamma = \int_0^\infty \int_0^{\frac{1}{2}\pi} \left(\frac{l}{\cos\theta}\right) \sin\theta \cos\theta\, g(l)\, d\theta\, dl.$$

Therefore
$$\gamma = S\langle l \rangle, \tag{3.11}$$

which equals the average total volume of slabs per unit volume of space.

From (3.10) and (3.11), the average 'pulse' length is

$$\langle w \rangle = 2\langle l \rangle; \tag{3.12}$$

S has cancelled out.

The above analyses show that γ and m (or n), the two independent quantities most easily measured from the single-wire signal $I(t)$ in the experiment, are simply related to moments of the random characteristic length of each of the three geometric classes [equations (3.2) and (3.3), (3.6) and (3.7) or (3.10) and (3.11), respectively].

If we were given a signal $I(t)$ and were told only that it was generated by traversing a random field of spheres or rods or slabs, could we identify the class from the measurements of γ and m? The answer is clearly no. Unfortunately, we cannot, for example, determine the moments of l from $I(t)$.

We can, however, determine the pulse-length moments $\langle w^k \rangle$ from $I(t)$. We might hope then that the moments $\langle l^q \rangle$ could be calculated from the pulse-length moments, but the calculation is not determinate. The moment relations turn out to be as follows.

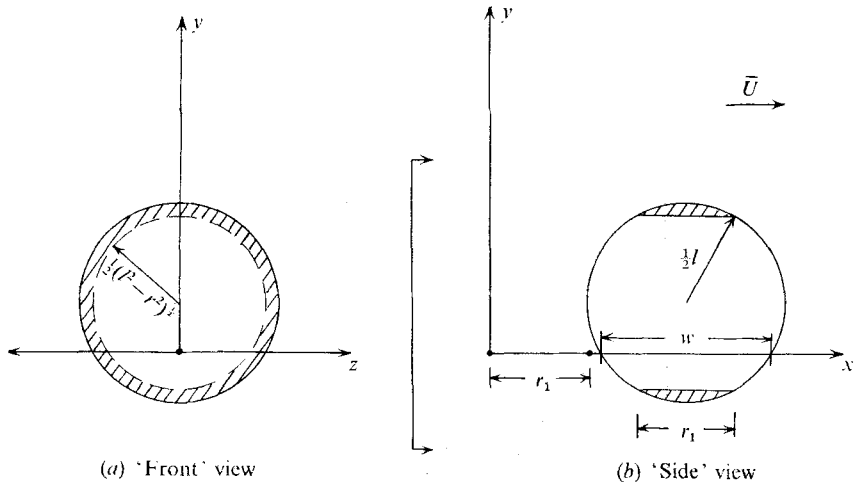

(*a*) 'Front' view (*b*) 'Side' view

FIGURE 10. Geometry for two-probe simultaneous detection (with spacing r_1 along x) of a sphere convected in the x direction. The shaded part of the sphere volume cannot be simultaneously detected by probes r_1 apart, for any position of the sphere centre.

(*a*) Sphere model: $$\langle w^k \rangle = \frac{2}{k+2} \frac{\langle l^{k+2} \rangle}{\langle l^2 \rangle}, \tag{3.13}$$

so that $\langle w \rangle = \frac{2}{3}\langle l^3 \rangle / \langle l^2 \rangle$, $\langle w^2 \rangle = \frac{1}{2}\langle l^4 \rangle / \langle l^2 \rangle$, etc.

(*b*) Cylinder model:

$$\langle w \rangle = \langle l^2 \rangle / \langle l \rangle, \quad \langle w^2 \rangle = \tfrac{4}{3}\langle l^3 \rangle / \langle l \rangle, \tag{3.14}$$

and $\langle w^k \rangle$ diverges for $k \geqslant 3$.

(*c*) Slab model: $$\langle w \rangle = 2\langle l \rangle, \tag{3.15}$$

and $\langle w^k \rangle$ diverges for $k \geqslant 2$.

In cases (*a*) and (*b*) above, the system of equations is not closed, i.e. there are more unknowns $\langle l^q \rangle$ than equations. In case (*c*) the result just serves to check (3.12); no new information is obtained. Therefore, *double- or multiple-probe detection must be used if we are to establish even this crude statistical geometric categorization.*

3.2. *Two-probe detection*

Since the statistical distributions of the 'fine-structure' regions in our three paradigms are homogeneous and isotropic, γ and n are the same for the signals from probes at all locations. For two probes 'operated' simultaneously, useful joint information is the probability that both lie within a single fine-structure region. Let $I_c(t)$ be a coincidence signal, defined to equal 1·0 during the time when both wires are inside the same fine-structure region and zero otherwise. Define γ_2, m_2 and $\langle w_2 \rangle$ or $I_c(t)$ in analogy to γ, m and $\langle w \rangle$ for $I(t)$.

(i) *Sphere model.* (*a*) *Two probes separated in the x direction by a distance* r_1. The probability that a sphere in the unit cube is detected by both probes simultaneously equals the projected area, on the y, z plane, of that part of the sphere with dimension w in the x direction greater than r_1, i.e.

$$\pi[(\tfrac{1}{2}l)^2 - (\tfrac{1}{2}r_1)^2]/(\text{unit area})$$

if $l \geqslant r_1$ and 0 if $l \leqslant r_1$, the area of a circle with radius $\frac{1}{2}(l^2 - r_1^2)^{\frac{1}{2}}$, as shown in figure 10. For convenience, the x, y plane is positioned so as to bisect the sphere. The expected number of spheres with diameters between l and $l + dl$ detected by both probes simultaneously is

$$\begin{cases} \frac{1}{4}\pi l^2(1 - r_1^2/l^2)\, g(l)\, dl & \text{if} \quad l \geqslant r_1, \\ 0 & \text{if} \quad l \leqslant r_1. \end{cases} \tag{3.16}$$

Therefore, the expected number of 'coincidence' events per unit distance is

$$\begin{aligned} m_2 &= \int_{r_1}^{\infty} \tfrac{1}{4}\pi l^2 \left(1 - \frac{r_1^2}{l^2}\right) g(l)\, dl, \\ &= \int_0^{\infty} \tfrac{1}{4}\pi l^2 \left(1 - \frac{r_1^2}{l^2}\right) g(l)\, dl - \int_0^{r_1} \tfrac{1}{4}\pi l^2 \left(1 - \frac{r_1^2}{l^2}\right) g(l)\, dl, \end{aligned}$$

which can be written as

$$m_2 = \tfrac{1}{4}\pi N \langle l^2 \rangle - \tfrac{1}{4}\pi N r_1^2 - \tfrac{1}{4}\pi N_{r_1} \langle l^2 \rangle_{r_1} + \tfrac{1}{4}\pi N_{r_1} r_1^2.$$

Dividing by equation (3.2),

$$\frac{m_2}{m} = 1 - \frac{r_1^2}{\langle l^2 \rangle} + \frac{N_{r_1}}{N}\left[\frac{r_1^2 - \langle l^2 \rangle_{r_1}}{\langle l^2 \rangle}\right]. \tag{3.17}$$

Since we should like to use $r_1/\langle w \rangle$ as a dimensionless variable, we divide the second term on the right by $\langle w \rangle^2$ and, using (3.4), multiply it by $\frac{4}{9}\langle l^3 \rangle^2 / \langle l^2 \rangle^3$:

$$\frac{m_2}{m} = 1 - \frac{4}{9}\frac{\langle l^3 \rangle^2}{\langle l^2 \rangle^3}\frac{r_1^2}{\langle w \rangle^2} + c_1(r_1), \tag{3.18}$$

where $c_1(r_1)$ represents the third term on the right-hand side of (3.17), which is of order r_1^3. To see this, note that

$N_{r_1} \equiv \int_0^{r_1} g(l)\, dl$ = the number of spheres in a unit volume with diameters $l \leqslant r_1$

and

$$\langle l^2 \rangle_{r_1} \equiv \frac{1}{N_{r_1}} \int_0^{r_1} l^2 g\, dl$$

= the average value of l^2 over those spheres with diameters $l \leqslant r_1$.

Since we plan to apply formulae like (3.17) only in the limit, it is convenient to rewrite (3.17) in a form which emphasizes the lowest power term in r_1. In order to do this, we must say something about the r_1 dependence of N_{r_1} and $\langle l^2 \rangle_{r_1}$. In the actual turbulence we expect that the relative number of fluid regions 'active' with fine-structure of any chosen size k^{-1} will decrease towards zero as l (the region size) approaches zero. In fact the physical picture makes sense only for $l > k^{-1}$. Therefore in our sphere, cylinder and slab paradigms we are interested in size probability density functions which behave like

$$\lim_{l \to 0} g(l) \sim l^b \quad (b > 1).$$

Suppose $b = 2$. Then the above definition of N_{r_1} shows 'small r_1^2' behaviour of the form $N_{r_1} \sim r_1^3 +$ higher powers, and $\langle l^2 \rangle_{r_1} \sim r_1^2 +$ higher powers.

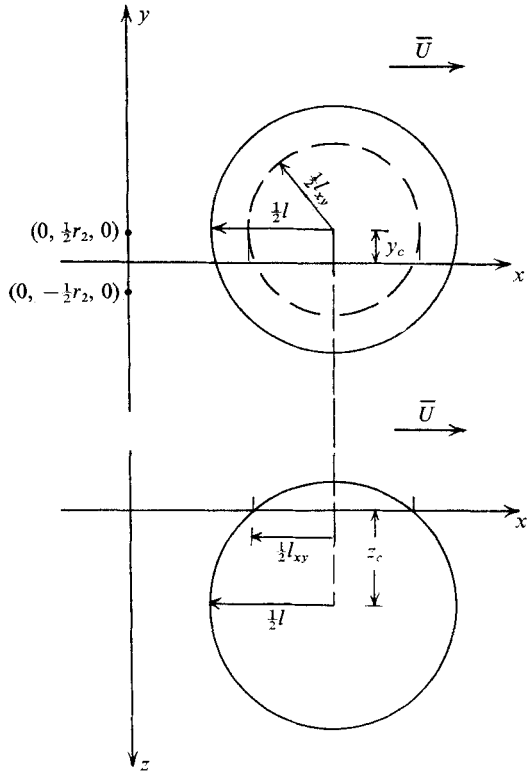

FIGURE 11. Geometry for two-probe simultaneous detection (with spacing r_2 along y) of a sphere convected in the x direction. The dashed circle is the intersection of sphere with x, y plane.

We conclude that (3.17) can be written as

$$m_2/m = 1 - r_1^2/\langle l^2\rangle + O(r_1^5). \tag{3.17a}$$

Next we turn to the calculation of γ_2. Let t_0 be the time when a probe at $(0, 0, 0)$ begins to register the sphere. Then it will stay in the sphere until time $t_0 + w/\overline{U}$. A probe at $(r_1, 0, 0)$ will register this sphere during the time interval from $t_0 + r_1/\overline{U}$ to $t_0 + r_1/\overline{U} + w/\overline{U}$. Therefore the probes will be simultaneously in the sphere from $t_0 + r_1/\overline{U}$ to $t_0 + w/\overline{U}$, if $w > r_1$. The corresponding values of w_2 are given by

$$w_2 = \begin{cases} w - r_1 = 2[(\frac{1}{2}l)^2 - y_c^2]^{\frac{1}{2}} - r_1 & \text{if} \quad w \geqslant r_1, \\ 0 & \text{if} \quad w \leqslant r_1. \end{cases}$$

Among those spheres identified by (3.16), the probability that their centres lie at a distance between y_c and $y_c + dy_c$ from the x axis is

$$\frac{2\pi y_c dy_c}{\pi[(\frac{1}{2}l)^2 - (\frac{1}{2}r_1)^2]}, \quad \text{for} \quad 0 \leqslant y_c \leqslant \tfrac{1}{2}[l^2 - r_1^2]^{\frac{1}{2}}.$$

Therefore,

$$\gamma_2 = \int_{r_1}^{\infty} \int_0^{\frac{1}{2}(l^2 - r_1^2)^{\frac{1}{2}}} \{2[(\tfrac{1}{2}l)^2 - y_c^2]^{\frac{1}{2}} - r_1\}\, 2\pi y_c g(l)\, dy_c\, dl$$

$$= \frac{\pi}{6} N\langle l^3\rangle \left[1 - \frac{3}{2}\frac{\langle l^2\rangle}{\langle l^3\rangle} r_1 + \frac{1}{2}\frac{r_1^3}{\langle l^3\rangle}\right] - \frac{\pi}{6} N_{r_1}\langle l^3\rangle_{r_1} \left[1 - \frac{3}{2}\frac{\langle l^2\rangle_{r_1}}{\langle l^3\rangle_{r_1}} r_1 + \frac{1}{2}\frac{r_1^3}{\langle l^3\rangle_{r_1}}\right].$$

From equations (3.3) and (3.4),

$$\left.\begin{aligned} \frac{\gamma_2}{\gamma} &= 1-\frac{r_1}{\langle w\rangle}+\frac{1}{2}\frac{r_1^3}{\langle l^3\rangle}-\frac{N_{r_1}}{N}\left[\frac{\frac{1}{2}r_1^3-\frac{3}{2}\langle l^2\rangle_r\, r_1+\langle l^3\rangle_{r_1}}{\langle l^3\rangle}\right], \\ \text{or}\qquad \gamma_2/\gamma &= 1-r_1/\langle w\rangle+\tfrac{1}{2}r_1^3/\langle l^3\rangle+c_2(r_1). \end{aligned}\right\} \tag{3.19}\dagger$$

If $g(l)\sim l^2+O(l^3)$, it turns out that $c_2(r_1)\sim r_1^6+\ldots$.

(*b*) *Two probes separated in the y direction by a distance* r_2. The probability $\beta(l;r_2)$ of a sphere in the unit cube being detected by both wires simultaneously equals the area on the y,z plane which the centre of the sphere may go through and still hit both wires.

If $l\leqslant r_2, \beta(l;r_2)=0$. If $l\geqslant r_2$, consider two probes, at $(0,\frac{1}{2}r_2,0)$ and $(0,-\frac{1}{2}r_2,0)$, and let a sphere pass through the y,z plane with its centre at (y_c,z_c).

In contrast to figure 10, this case is properly illustrated by a sphere whose centre lies on none of the co-ordinate planes. In figure 11, the sphere [with centre at (x,y_c,z_c)] is cut by the x,y plane in a circle of radius

$$\tfrac{1}{2}l_{xy}=[(\tfrac{1}{2}l)^2-z_c^2]^{\frac{1}{2}}.$$

To evaluate
$$\beta(l;r_2)=\iint_{\text{Area}} dy_c\,dz_c\Big/\text{unit area},$$

the limits of integration must be determined. By putting $l_{xy}=r_2$, the smallest circle in the x,y plane to hit both probes simultaneously, the limits on z_c may be found:

$$l_{xy}=r_2=2[(\tfrac{1}{2}l)^2-(z_c)^2_{\max}]^{\frac{1}{2}},$$

so
$$-[(\tfrac{1}{2}l)^2-(\tfrac{1}{2}r_2)^2]^{\frac{1}{2}}\leqslant z_c\leqslant[(\tfrac{1}{2}l)^2-(\tfrac{1}{2}r_2)^2]^{\frac{1}{2}}.$$

With given z_c in this range, the maximum of y_c is determined by the wire at $(0,-\frac{1}{2}r_2,0)$ and the minimum by the wire at $(0,\frac{1}{2}r_2,0)$:

$$-\{[(\tfrac{1}{2}l)^2-z_c^2]^{\frac{1}{2}}-\tfrac{1}{2}r_2\}\leqslant y_c\leqslant[(\tfrac{1}{2}l)^2-z_c^2]^{\frac{1}{2}}-\tfrac{1}{2}r_2.$$

Therefore
$$\beta(l;r_2)=4\int_0^{[(\frac{1}{2}l)^2-(\frac{1}{2}r_2)^2]^{\frac{1}{2}}}\int_0^{[(\frac{1}{2}l)^2-z_c^2]^{\frac{1}{2}}-\frac{1}{2}r_2} dy_c\,dz_c,$$

which turns out to be

$$\beta(l;r_2)=\frac{\pi l^2}{4}\left\{1-\frac{4}{\pi}\frac{r_2}{l}+O\left[\left(\frac{r_2}{l}\right)^3\right]\right\}. \tag{3.20}$$

The expected number of spheres with diameters between l and dl detected by both probes simultaneously is $\beta(l;r_2)g(l)\,dl$, so

$$\begin{aligned} m_2&=\int_{r_2}^{\infty}\beta(l;r_2)g(l)\,dl \\ &=\frac{4}{\pi}N\left[\langle l^2\rangle-\frac{4}{\pi}\langle l\rangle r_2\right]-\frac{\pi}{4}N_{r_2}\left[\langle l^2\rangle_{r_2}-\frac{4}{\pi}\langle l\rangle_{r_2}r_2\right]+O\left[{}_{r_2}N_{r_2}\left\langle\frac{1}{l}\right\rangle r_2^3\right]. \end{aligned}$$

† We have not bothered to normalize the r_1^3 term with $\langle w\rangle^3$ because we shall later neglect it.

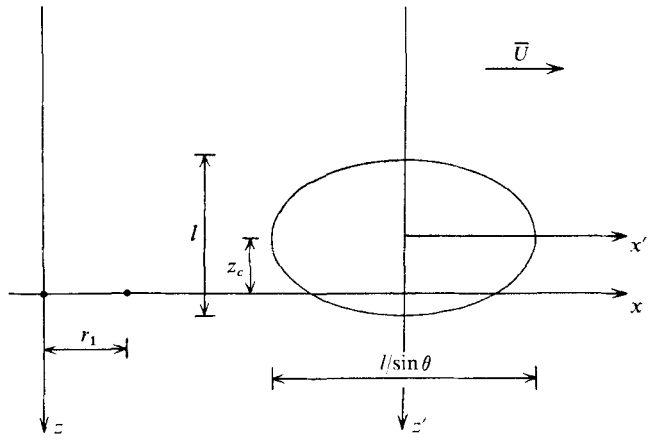

FIGURE 12. Intersection with x, z plane of the cylinder sketched in figure 8.

With equations (3.2) and (3.4),

$$\left.\begin{aligned}\frac{m_2}{m} &= 1-\frac{8}{3\pi}\frac{\langle l\rangle\langle l^3\rangle}{\langle l^2\rangle^2}\frac{r_2}{\langle w\rangle}+\frac{N_{r_2}[(4/\pi)\langle l\rangle_{r_2}r_2-\langle l^2\rangle_{r_2}]}{N\langle l^2\rangle}\\ &\quad+O\left[\frac{r_2N}{N}\,{}_{r_2}\!\left\langle\frac{1}{l}\right\rangle\frac{r_2^3}{\langle l^2\rangle}\right],\\ \text{or}\qquad \frac{m_2}{m} &= 1-\frac{8}{3\pi}\frac{\langle l\rangle\langle l^3\rangle}{\langle l^2\rangle^2}\frac{r_2}{\langle w\rangle}+c_3(r_2).\end{aligned}\right\} \tag{3.21}$$

Here, $${}_{r_2}N\equiv\int_{r_2}^{\infty}g(l)\,dl=N-N_{r_2}\quad\text{and}\quad {}_{r_2}\!\left\langle\frac{1}{l}\right\rangle\equiv\frac{1}{{}_{r_2}N}\int_{r_2}^{\infty}\frac{1}{l}g(l)\,dl.$$

For $g(l)\sim l^2+\ldots$, we can estimate $c_3(r_2)\sim r_2^3+\ldots$.

The analysis for $\gamma_2(r_2)$ shows that the dependence of γ_2 on r_2 is exactly the same as its dependence on r_1. This is simply a consequence of isotropy, and applies to any isotropic binary field, including blobs, rods and slabs. With isotropy, γ_2 depends on the distance between the two probes only.

(ii) *Cylinder model.* (*a*) *Two probes separated in the x direction by a distance* r_1. The probability that a unit length of cylinder is detected by both probes simultaneously equals the projected area on the y,z plane of that part of this unit segment with dimension in the x direction greater than r_1. Referring to figure 8, the projection is a rectangle with length $\sin\theta$ in the y direction. Since the y axis is oriented so that the cylinder is parallel to the x,y plane, the cylinder is cut by the x,z plane in to an ellipse, shown in figure 12. Its equation is

$$\frac{x'^2}{(l/2\sin\theta)^2}+\frac{z'^2}{(\frac{1}{2}l)^2}=1.$$

The extreme values of z_c may be obtained by substituting $x'=\frac{1}{2}r_1$ in the above equation:

$$(z_c)_{\text{ext.}}=\begin{cases}\pm[(\frac{1}{2}l)^2-(\frac{1}{2}r_1\sin\theta)^2]^{\frac{1}{2}} & \text{if } \begin{cases}l\geqslant r_1,\\ l\leqslant r_1\end{cases}\text{ and } \theta\leqslant\sin^{-1}(l/r_1),\\ 0 & \text{if } l\leqslant r_1 \text{ and } \theta\geqslant\sin^{-1}(l/r_1).\end{cases}$$

Then the simultaneous hit probability for a single θ value is

$$(\text{unit length}) \times 2\sin\theta[(\tfrac{1}{2}l)^2-(\tfrac{1}{2}r_1\sin\theta)^2]/\text{unit area}.$$

Since the orientation of cylinders is assumed to be statistically isotropic, the probability density of θ is the measure of relative solid angle corresponding to θ, i.e.

$$p_\theta(\theta) = \begin{cases} \sin\theta & \text{for} \quad 0 \leqslant \theta \leqslant \tfrac{1}{2}\pi, \\ 0 & \text{otherwise.} \end{cases}$$

The expected number of cylinders hitting both probes simultaneously, with diameters between l and $l+dl$ and orientation angles between θ and $\theta+d\theta$, is

$$\left.\begin{cases} g(l)\times 2\sin^2\theta[(\tfrac{1}{2}l)^2-(\tfrac{1}{2}r_1\sin\theta)^2]^{\frac{1}{2}}d\theta\,dl & \text{if} \quad l \geqslant r_1 \quad \text{and} \quad 0 \leqslant \theta \leqslant \tfrac{1}{2}\pi, \\ & \text{or} \quad l \leqslant r_1 \quad \text{and} \quad 0 \leqslant \theta \leqslant \sin^{-1}(l/r_1), \\ 0 & \text{if} \quad l \leqslant r_1 \quad \text{and} \quad \theta \geqslant \sin^{-1}(l/r_1). \end{cases}\right\} \tag{3.22}$$

Now,
$$\begin{aligned} m_2 &= \int_{r_1}^{\infty}\int_0^{\frac{1}{2}\pi} 2g(l)\sin^2\theta[(\tfrac{1}{2}l)^2-(\tfrac{1}{2}r_1\sin\theta)^2]^{\frac{1}{2}}d\theta\,dl \\ &\quad + \int_0^{r_1}\int_0^{\sin^{-1}(l/r_1)} 2g(l)\sin^2\theta[(\tfrac{1}{2}l)^2-(\tfrac{1}{2}r_1\sin\theta)^2]^{\frac{1}{2}}d\theta\,dl \\ &= \frac{\pi}{4}L\langle l\rangle - \frac{3\pi}{32}L\left\langle\frac{1}{l}\right\rangle r_1^2 + L_{r_1}\left[\frac{3\pi}{32}\left\langle\frac{1}{l}\right\rangle_{r_1} r_1^2 - \frac{\pi}{4}\langle l\rangle_{r_1} + O\left(\frac{\langle l^4\rangle_{r_1}}{r_1^3}\right)\right] \\ &\quad + O\left[r_1 L_{r_1}\left\langle\frac{1}{l^3}\right\rangle r_1^4\right]. \end{aligned}$$

Here
$$L_{r_1} \equiv \int_0^{r_1} g(l)\,dl, \quad \langle l\rangle_{r_1} \equiv \frac{1}{L_{r_1}}\int_0^{r_1} l g(l)\,dl$$

and
$${}_{r_1}L \equiv \int_{r_1}^{\infty} g(l)\,dl = L - L_{r_1}, \quad \left\langle\frac{1}{l^3}\right\rangle_{r_1} \equiv \frac{1}{{}_{r_1}L}\int_{r_1}^{\infty}\frac{1}{l^3}g(l)\,dl.$$

From (3.6) and (3.8),

$$\left.\begin{aligned} \frac{m_2}{m} &= 1 - \frac{3}{8}\frac{\langle l^2\rangle^2}{\langle l^3\rangle}\left\langle\frac{1}{l}\right\rangle\frac{r_1^2}{\langle w\rangle^2} + \frac{L_{r_1}}{L\langle l\rangle}\left[\frac{3}{8}\left\langle\frac{1}{l}\right\rangle_{r_1} r_1^2\langle l\rangle_{r_1} + O\left(\frac{\langle l^4\rangle_{r_1}}{r_1^3}\right)\right] \\ &\quad + O\left[\frac{r_1 L}{L}\,{}_{r_1}\left\langle\frac{1}{l^3}\right\rangle\frac{r_1^4}{\langle l\rangle}\right], \\ \text{or} \quad \frac{m_2}{m} &= 1 - \frac{3}{8}\frac{\langle l^2\rangle^2}{\langle l^3\rangle}\left\langle\frac{1}{l}\right\rangle\frac{r_1^2}{\langle w\rangle^2} + c_4(r_1). \end{aligned}\right\} \tag{3.23}$$

If $g(l) \sim l^2+\ldots$, it turns out that $c_4(r_1) \sim r_1^4+\ldots$.

From figure 8 we find that, with the second probe at $(r_1, 0, 0)$, the corresponding w_2 (for both probes inside the cylinder) is

$$w_2 = \begin{cases} w - r_1 = (2/\sin\theta)\,[(\tfrac{1}{2}l)^2 - z_c^2]^{\frac{1}{2}} - r_1 & \text{if} \quad w \geqslant r_1, \\ 0 & \text{if} \quad w \leqslant r_1. \end{cases}$$

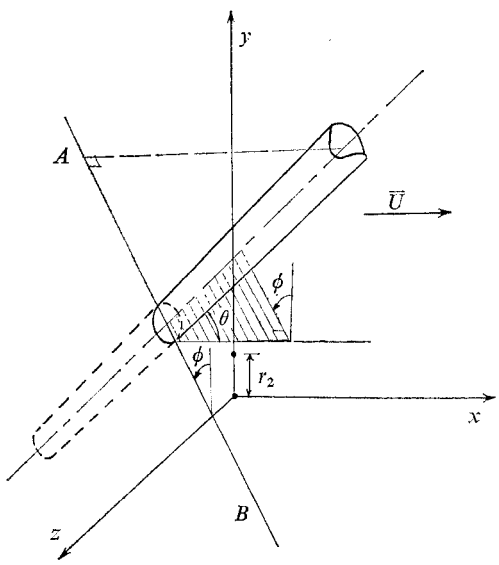

FIGURE 13. Cylinder with general orientation. As it is convected in the x direction, its intersection with the y, z plane travels along the line AB.

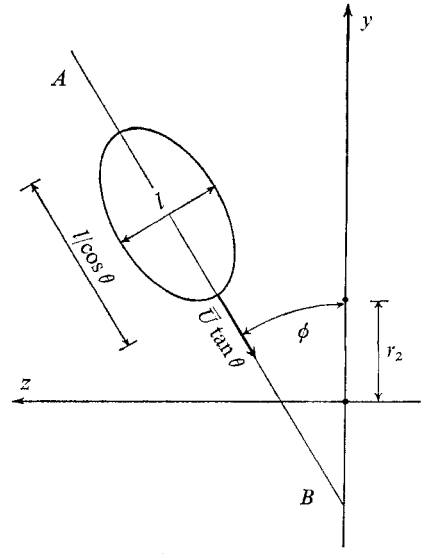

FIGURE 14. Elliptical intersection of the circular cylinder of figure 13 with the y, z plane.

Among those cylinders identified by (3.22), the probability that their axes are located at a distance between z_c and z_c+dz_c from the x, y plane is

$$\begin{cases} \frac{1}{2}[(\frac{1}{2}l)^2-(\frac{1}{2}r_1\sin\theta)^2]^{-\frac{1}{2}}dz_c & \text{if} \quad |z_c| \leqslant [(\frac{1}{2}l)^2-(\frac{1}{2}r_1\sin\theta)^2]^{\frac{1}{2}}, \\ 0 & \text{otherwise.} \end{cases}$$

Thus,

$$\gamma_2 = 2\int_{r_1}^{\infty}\int_0^{\frac{1}{2}\pi}\int_0^{[(\frac{1}{2}l)^2-(\frac{1}{2}r_1\sin\theta)^2]^{\frac{1}{2}}}\left\{\frac{2}{\sin\theta}\left[\left(\frac{l}{2}\right)^2-z_c^2\right]^{\frac{1}{2}}-r_1\right\}g(l)\sin^2\theta\,dz_c\,d\theta\,dl$$
$$+2\int_0^{r_1}\int_0^{\sin^{-1}(l/r_1)}\int_0^{[(\frac{1}{2}l)^2-(\frac{1}{2}r_1\sin\theta)^2]^{\frac{1}{2}}}\left\{\frac{2}{\sin\theta}\left[\left(\frac{l}{2}\right)^2-z_c^2\right]^{\frac{1}{2}}-r_1\right\}g(l)\sin^2\theta\,dz_c\,d\theta\,dl,$$

which turns out to be

$$\gamma_2 = \tfrac{1}{4}\pi L\langle l^2\rangle - \tfrac{1}{4}\pi L\langle l\rangle r_1 + \tfrac{1}{4}\pi L_{r_1}[\langle l\rangle_{r_1}r_1 - \langle l^2\rangle_{r_1} + O(\langle l^4\rangle_{r_1}/r_1^2)] + O[_{r_1}L_{r_1}\langle 1/l\rangle r_1^3].$$

From (3.7) and (3.8),

$$\left.\begin{aligned} \frac{\gamma_2}{\gamma} &= 1-\frac{r_1}{\langle w\rangle}+\frac{L_{r_1}}{L\langle l^2\rangle}\left[\langle l\rangle_{r_1}r_1-\langle l^2\rangle_{r_1}+O\left(\frac{\langle l^4\rangle_{r_1}}{r_1^2}\right)\right]+O\left[\frac{r_1 L}{L}{}_{r_1}\left\langle\frac{1}{l}\right\rangle\frac{r_1^3}{\langle l^2\rangle}\right], \\ \text{or} \quad & \gamma_2/\gamma = 1-r_1/\langle w\rangle + c_5(r_1). \end{aligned}\right\} \tag{3.24}$$

For $g(l) \sim l^2+\ldots$, $c_5(r_1) \sim r_1^3+\ldots$.

(*b*) *Two probes separated in the y direction by a distance* r_2. Here we cannot specialize to a case with the x, y plane set parallel to the cylinder axis, as in figures 8 and 12. Figure 13 shows a cylinder convected along the x direction with its axis at an angle θ to the x axis and its projection on the y, z plane at an angle ϕ to the y axis. The cylinder is cut by the y, z plane in an ellipse, shown in figure 14.

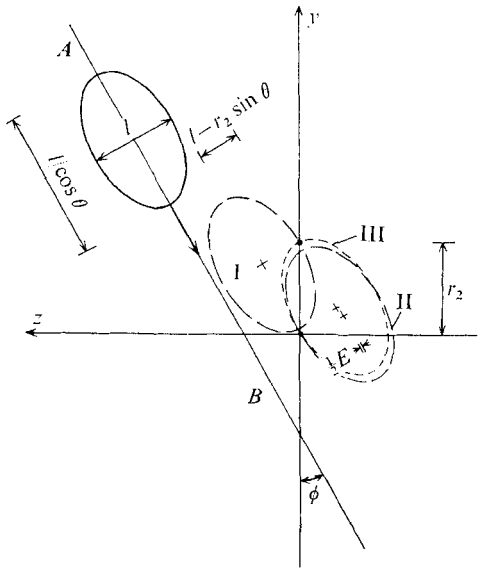

FIGURE 15. Some extreme cases for simultaneous detection of the cylinder, with probes at (0, 0, 0) and $(0, r_2, 0)$. The cylinder axes are all parallel to that in figures 13 and 14.

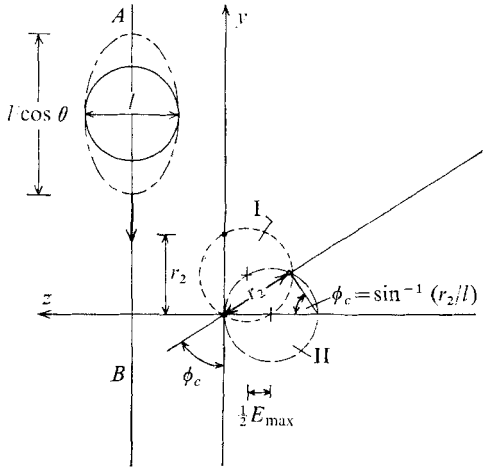

FIGURE 16. Intersection of cylinder with y, z plane in the asymptotic case of $\theta \to 0$. Dashed circles show simultaneous detection limits for different possible cylinder axis positions, all with $\theta \to 0$.

As the cylinder translates in the x direction with velocity $\bar{U}$, the ellipse moves along the line AB with velocity $\bar{U}\tan\theta$. The probability that a unit length of this cylinder hits both probes simultaneously equals the area on the y, z plane which the mid-point of this unit axis of the cylinder may go through and still have its bulk enclose both probes simultaneously. This area is a rectangle of length $\sin\theta$ along the AB direction and width $l - r_2\sin\phi - E(\theta, \phi, r_2, l)$. Figure 15 shows that $l - r_2\sin\phi$ is the distance over which the axis of the cylinder may shift perpendicular to AB and still hit both probes, but we seek cases in which it hits both probes simultaneously. The term E (not written out explicitly) subtracts the

part of $l - r_2 \sin\phi$ for which the hits are *not* simultaneous. Therefore the probability for simultaneous envelopment is proportional to

$$(\text{unit length}) \times \{\sin\theta[l - r_2\sin\phi - E(\theta, \phi, r_2, l]\}/(\text{unit area}).$$

Figure 16 shows that there is a maximum value of E when $\phi = 0$ or π, and $\theta \to 0$, at which

$$E_{\max} = O(l.r_2^2/l^2).$$

Also, for $\theta \to 0$, $E = 0$ if $\phi \geqslant \sin^{-1}(r_2/l) \equiv \phi_c$† or $\pi - \phi \geqslant \sin^{-1}(r_2/l)$. Then the contribution from the integration of E is at least of the order of r_2^3.

Since the orientation of cylinders is isotropic, the probability density of θ is

$$\begin{cases} \sin\theta & \text{if} \quad 0 \leqslant \theta \leqslant \frac{1}{2}\pi, \\ 0 & \text{otherwise,} \end{cases}$$

and the probability density of ϕ is

$$\begin{cases} 1/\pi & \text{if} \quad 0 \leqslant \phi \leqslant \pi, \\ 0 & \text{otherwise.} \end{cases}$$

The expected number of cylinders hitting both wires simultaneously, with diameters between l and $l + dl$, and orientation angles between θ and $\theta + d\theta$ and ϕ and $\phi + d\phi$, is $(1/\pi)\sin^2\theta(l - r_2\sin\phi)g(l)\,d\phi\,d\theta\,dl$ + higher order terms, for $0 \leqslant \theta \leqslant \frac{1}{2}\pi$ and $0 \leqslant \phi \leqslant \pi$ if $l \geqslant r_2$, or $\phi \leqslant \sin^{-1}(l/r_2)$ or $\pi - \phi \leqslant \sin^{-1}(l/r_2)$ if $l \leqslant r_2$. Therefore,

$$m_2 = \int_{r_2}^{\infty}\int_0^{\pi}\int_0^{\frac{1}{2}\pi} \frac{1}{\pi}\sin^2\theta(l - r_2\sin\phi)g(l)\,d\theta\,d\phi\,dl$$
$$+ 2\int_0^{r_2}\int_0^{\sin^{-1}(l/r_2)}\int_0^{\frac{1}{2}\pi} \frac{1}{\pi}\sin^2\theta(l - r_2\sin\phi)g(l)\,d\theta\,d\phi\,dl + O\left(L\left\langle\frac{1}{l^2}\right\rangle r_2^3\right),$$

so $$m_2 = \tfrac{1}{4}\pi L\langle l\rangle - \tfrac{1}{2}Lr_2 + \tfrac{1}{4}L_{r_2}[2r_2 - \pi\langle l\rangle_{r_2} + O(\langle l^2\rangle_{r_2}/r_2)] + O(L\langle 1/l^2\rangle r_2^3).$$

From (3·6) and (3·8),

$$\left.\begin{aligned} &\frac{m_2}{m} = 1 - \frac{2}{\pi}\frac{\langle l^2\rangle}{\langle l\rangle^2}\frac{r_2}{\langle w\rangle} + \frac{L_{r_2}}{L\langle l\rangle}\left[\frac{2}{\pi}r_2 - \langle l\rangle_{r_2} + O\left(\frac{\langle l^2\rangle_{r_2}}{r_2}\right)\right] + O\left(\left\langle\frac{1}{l^2}\right\rangle\frac{r_2^3}{\langle l\rangle}\right), \\ \text{or} \quad &\frac{m_2}{m} = 1 - \frac{2}{\pi}\frac{\langle l^2\rangle}{\langle l\rangle^2}\frac{r_2}{\langle w\rangle} + c_6(r_2). \end{aligned}\right\} \tag{3.25}$$

For $g(l) \sim l^2 + \ldots$, $c_6(r_2) \sim r_2^3 + \ldots$.

(iii) *Slab model.* (*a*) *Two probes separated in the x direction by a distance* r_1. If a second probe is at $(r_1, 0, 0)$, see figure 9, the probability that the volume under a unit area of a slab is detected by both probes simultaneously equals the projected area on the y, z plane of that part of this unit slab with dimension in the x direction greater than r_1, i.e.

$$\begin{cases} \cos\theta & \text{if} \quad w \geqslant r_1, \quad \text{i.e.} \begin{cases} l \geqslant r_1, & 0 \leqslant \theta \leqslant \frac{1}{2}\pi, \\ \text{or} \quad l \leqslant r_1, & \cos^{-1}(l/r_1) \leqslant \theta \leqslant \frac{1}{2}\pi, \end{cases} \\ 0 & \text{otherwise.} \end{cases}$$

† ϕ_c (see figure 16) is a minimum only for the $\theta \to 0$ case; in the general case (figure 15) the minimum value of ϕ will be smaller than ϕ_c.

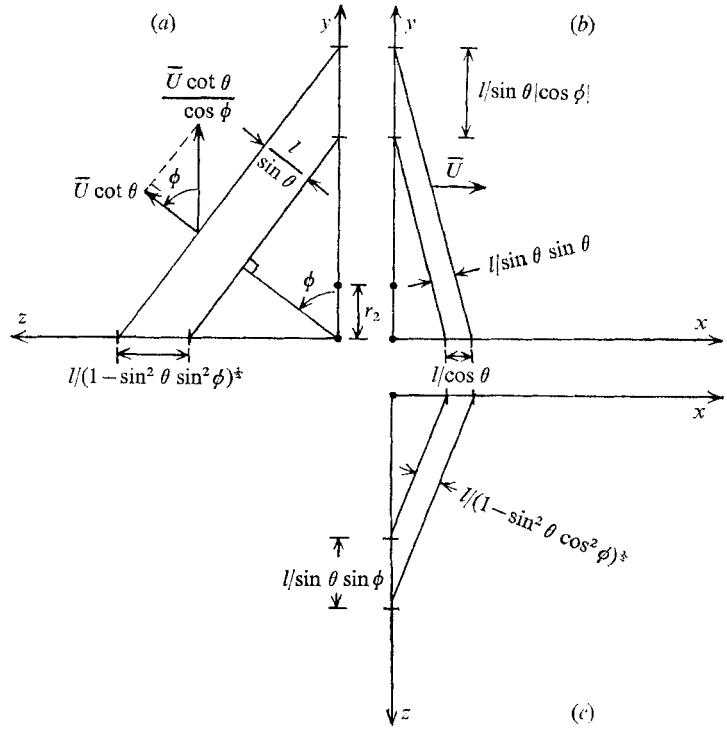

FIGURE 17. Intersection of an infinite slab with the three Cartesian axis planes. It is being convected in the x direction and detected by probes at (0, 0, 0) and (0, r_2, 0).

Since the orientation of slabs is isotropic, the probability density of angle θ is the measure of relative solid angle corresponding to θ, i.e.

$$\begin{cases} \sin\theta & \text{if} \quad 0 \leqslant \theta \leqslant \tfrac{1}{2}\pi, \\ 0 & \text{otherwise.} \end{cases}$$

Therefore,

$$m_2 = \int_{r_1}^{\infty}\int_0^{\frac{1}{2}\pi} \sin\theta\cos\theta g(l)\,d\theta\,dl + \int_0^{r_1}\int_{\cos^{-1}(l/r_1)}^{\frac{1}{2}\pi} \sin\theta\cos\theta g(l)\,d\theta\,dl,$$

so
$$m_2 = \tfrac{1}{2}S - \tfrac{1}{2}S_{r_1}[1 - \langle l^2\rangle_{r_1}/r_1^2],$$

and, from (3.10),
$$\frac{m_2}{m} = 1 - \frac{S_{r_1}}{S}\left[1 - \frac{\langle l^2\rangle_{r_1}}{r_1^2}\right],$$

or
$$m_2/m = 1 - c_7(r_1). \qquad (3.26)$$

If $g(l) \sim l^2 + \ldots$, it turns out that $c_7(r_1) \sim r_1^3 + \ldots$.

The corresponding w_2 for both probes inside the slab is given by

$$w_2 = \begin{cases} w - r_1 = \dfrac{l}{\cos\theta} - r_1 & \text{if} \quad \begin{cases} l \geqslant r_1, \\ \text{or} \quad l \leqslant r_1, \cos^{-1}(l/r_1) \leqslant \theta \leqslant \tfrac{1}{2}\pi, \end{cases} \\ 0 \qquad\qquad\qquad\qquad\quad \text{otherwise.} \end{cases}$$

Therefore,
$$\gamma_2 = \int_{r_1}^{\infty}\int_0^{\frac{1}{2}\pi}\left(\frac{l}{\cos\theta}-r_1\right)\cos\theta\sin\theta g(l)\,d\theta\,dl + \int_0^{r_1}\int_{\cos^{-1}(l/r_1)}^{\frac{1}{2}\pi}\left(\frac{l}{\cos\theta}-r_1\right)\cos\theta\sin\theta g(l)\,d\theta\,dl,$$

so
$$\gamma_2 = S\langle l\rangle - \tfrac{1}{2}Sr_1 + \tfrac{1}{2}S_{r_1}[r_1 - 2\langle l\rangle_{r_1} + \langle l^2\rangle_{r_1}/r_1].$$

From (3.11) and (3.12),

$$\left.\begin{aligned}\frac{\gamma_2}{\gamma} &= 1-\frac{r_1}{\langle w\rangle}+\frac{S_{r_1}}{2S\langle l\rangle}\left[r_2-2\langle l\rangle_{r_1}+\frac{\langle l^2\rangle_{r_1}}{r_1}\right],\\ \text{or}\quad \gamma_2/\gamma &= 1-r_1/\langle w\rangle + c_8(r_1).\end{aligned}\right\} \tag{3.27}$$

if $g(l)\sim l^2+\ldots$, it turns out that $c_8(r_1)\sim r_1^4+\ldots$.

(*b*) *Two probes separated in the y direction by a distance* r_2. Let us suppose that a slab is convected along the x direction with its normal at an angle θ to the x axis and its projection on the y,z plane at an angle ϕ to the y axis. The slab is cut into strips by all three planes as shown in figure 17. The slabs are infinite, so all certainly hit a probe (except for a set of measure zero). Suppose that a slab encloses the probe at the origin. Then the probability that it hits both simultaneously is

$$\begin{cases}1 & \text{if } \ l/\sin\theta|\cos\phi| \geqslant r_2,\\ 0 & \text{if } \ l/\sin\theta|\cos\phi| \leqslant r_2,\end{cases}$$

i.e.

$$\begin{cases}1 & \text{if } \begin{cases}l\geqslant r_2, & 0\leqslant\theta\leqslant\frac{1}{2}\pi, \quad 0\leqslant\phi\leqslant\pi,\\ l<r_2, & 0\leqslant\theta\leqslant\sin^{-1}(l/r_2), \quad 0\leqslant\phi\leqslant\pi,\\ l<r_2, & \theta>\sin^{-1}(l/r_2), \quad \cos^{-1}(l/r_2\sin\theta)<\phi<\pi-\cos^{-1}(l/r_2\sin\theta),\end{cases}\\ 0 & \text{otherwise.}\end{cases}$$

As in (3.9), the expected number of slabs hitting one probe, with thickness between l and $l+dl$, and orientation angles between θ and $\theta+d\theta$, and ϕ and $\phi+d\phi$, is

$$(1/\pi)\sin\theta\cos\theta g(l)\,d\phi\,d\theta\,dl.$$

Therefore,

$$\begin{aligned}m_2 &= \int_{r_2}^{\infty}\int_0^{\frac{1}{2}\pi}\int_0^{\pi}\frac{1}{\pi}\sin\theta\cos\theta g(l)\,d\phi\,d\theta\,dl\\ &\quad+\int_0^{r_2}\int_0^{\sin^{-1}(l/r_2)}\int_0^{\pi}\frac{1}{\pi}\sin\theta\cos\theta g(l)\,d\phi\,d\theta\,dl\\ &\quad+2\int_0^{r_2}\int_{\sin^{-1}(l/r_2)}^{\frac{1}{2}\pi}\int_{\cos^{-1}(l/r_2\sin\theta)}^{\frac{1}{2}\pi}\frac{1}{\pi}\sin\theta\cos\theta g(l)\,d\phi\,d\theta\,dl,\\ &= \tfrac{1}{2}S-\tfrac{1}{2}S_{r_2}\left[1-\frac{4}{\pi}\frac{\langle l\rangle_{r_2}}{r_2}+\left(\frac{4}{\pi}-1\right)\frac{\langle l^2\rangle_{r_2}}{r_2^2}+O\left(\frac{\langle l^3\rangle_{r_2}}{r_2^3}\right)\right].\end{aligned}$$

From (3.10),

$$\left.\begin{aligned}\frac{m_2}{m} &= 1-\frac{S_{r_2}}{S}\left[1-\frac{4}{\pi}\frac{\langle l\rangle_{r_2}}{r_2}+\left(\frac{4}{\pi}-1\right)\frac{\langle l^2\rangle_{r_2}}{r_2^2}+O\left(\frac{\langle l^3\rangle_{r_2}}{r_2^3}\right)\right],\\ \text{or}\quad m_2/m &= 1-c_9(r_2).\end{aligned}\right\} \tag{3.28}$$

If $g(l)\sim l^2+\ldots$, it turns out that $c_9(r_2)\sim r_2^3+\ldots$.

For convenience we summarize the analytical results in tables 1 and 2.

	Property		
Model	m	γ	$\langle w\rangle = \gamma/m$
Spheres	$\frac{1}{4}\pi N\langle l^2\rangle$	$\frac{1}{6}\pi N\langle l^3\rangle$	$\frac{2}{3}\langle l^3\rangle/\langle l^2\rangle$
Cylinders	$\frac{1}{4}\pi L\langle l\rangle$	$\frac{1}{4}\pi L\langle l^2\rangle$	$\langle l^2\rangle/\langle l\rangle$
Slabs	$\frac{1}{2}S$	$S\langle l\rangle$	$2\langle l\rangle$

TABLE 1. Theoretical properties as determined from single-probe responses to the three simple geometric models for 'blobs', 'rods' and 'slabs'

	Behaviour for 'small' separation	
Model	$m_2/m = n_2/n$	γ_2/γ
Spheres	$1-\frac{4}{9}\frac{\langle l^3\rangle^2}{\langle l^2\rangle^3}\frac{r_1^2}{\langle w\rangle^2}+c_1(r_1)$	$1-\frac{r_{1,2}}{\langle w\rangle}+\frac{1}{2}\frac{r_{1,2}^3}{\langle l^3\rangle}+c_2(r_{1,2})$
	$1-\frac{8}{3\pi}\frac{\langle l\rangle\langle l^3\rangle}{\langle l^2\rangle^2}\frac{r_2}{\langle w\rangle}+c_3(r_2)$	
Cylinders	$1-\frac{3}{8}\frac{\langle l^2\rangle^2}{\langle l^3\rangle}\left\langle\frac{1}{l}\right\rangle\frac{r_1^2}{\langle w\rangle^2}+c_4(r_1)$	$1-\frac{r_{1,2}}{\langle w\rangle}+c_5(r_{1,2})$
	$1-\frac{2}{\pi}\frac{\langle l^2\rangle}{\langle l\rangle^2}\frac{r_2}{\langle w\rangle}=c_6(r_2)$	
Slabs	$1-c_7(r_1)$	$1-\frac{r_{1,2}}{\langle w\rangle}+c_8(r_{1,2})$
	$1-c_9(r_2)$	

TABLE 2. Theoretical behaviour of two-probe coincidence functions for vanishingly small probe separations in the three geometric models

$c_1(r) \sim r^5+\ldots$	$c_6(r) \sim r^3+\ldots$
$c_2(r) \sim r^6+\ldots$	$c_7(r) \sim r^3+\ldots$
$c_3(r) \sim r^3+\ldots$	$c_8(r) \sim r^4+\ldots$
$c_4(r) \sim r^4+\ldots$	$c_9(r) \sim r^3+\ldots$
$c_5(r) \sim r^3+\ldots$	

TABLE 3. $r \to 0$ behaviour of the c's, assuming that $g(l) \sim l^2+$higher order terms

The lowest powers of r_1 or r_2 in c_1, c_2, etc., estimated under the assumption that $g(l) \sim l^2+$ higher order terms, are summarized in table 3. The plan is to compare turbulent fine-structure-region measurements of $m_2(r_1,0)/m, m_2(0,r_2)/m, \gamma_2(r_1,0)/\gamma$ and $\gamma_2(0,r_2)/\gamma$ with the $r\to 0$ behaviour of the three geometric categories as summarized in table 2. The hope is that the data will show a preference. Of course the uncertainties of the c's render comparisons with the m_2/m form estimated for 'slabs' almost meaningless. The $r\to 0$ form of the c_i's as tabulated above have been designed to give as low a power of r as seems plausible. We assumed $g(l) \sim l^2+\ldots$, but it is quite possible that $g(l) \sim l^\rho+\ldots$ with $\rho > 2$, in which case the c_i's would start with higher powers of r.

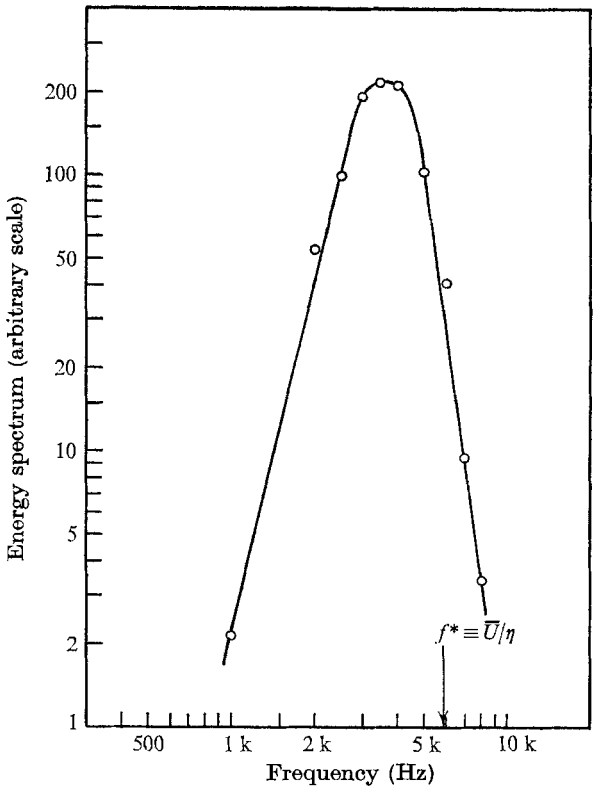

FIGURE 18. Measured one-dimensional spectrum of the filtered signal whose intermittent properties are being measured.

4. Experimental results

It is assumed in the analyses of § 3 that both the overlap of the fine-structure regions and the probability that two separate regions hit the two probes simultaneously are negligible. To meet these assumptions it is necessary to have the fraction of space occupied by the fine-structure as small as possible, i.e. to have a filtered signal with a small intermittency factor γ. If the intermittency factor is too small, however, the measurements of the coincidence functions γ_2 and n_2 are inaccurate. A compromise value of $\gamma = 0{\cdot}2 \sim 0{\cdot}4$ was chosen, and the cut-off frequency of the high-pass filter was determined with the aid of the intermittency measurements of band-pass signals described in I. The energy spectrum of the filtered signal (figure 18) has a peak at 3·5 kHz (Kolmogorov-scale frequency $f^* \equiv \bar{U}/\eta = 5{\cdot}9\,\text{kHz}$), which corresponds to a length scale $\eta_f = 2{\cdot}26 \times 10^{-2}\,\text{in.}$

The results of single-probe measurements of the high-pass signal are

$$\gamma = 0{\cdot}3, \quad n = 750\,\text{s}^{-1}, \quad \langle w \rangle = 0{\cdot}2\,\text{in.}, \quad m = 1{\cdot}5\,\text{in.}^{-1}. \tag{4.1}$$

For any isotropic surface geometry, Corrsin (1955) has shown that the average surface σ per unit volume is related to m by

$$\sigma = 2m. \tag{4.2}$$

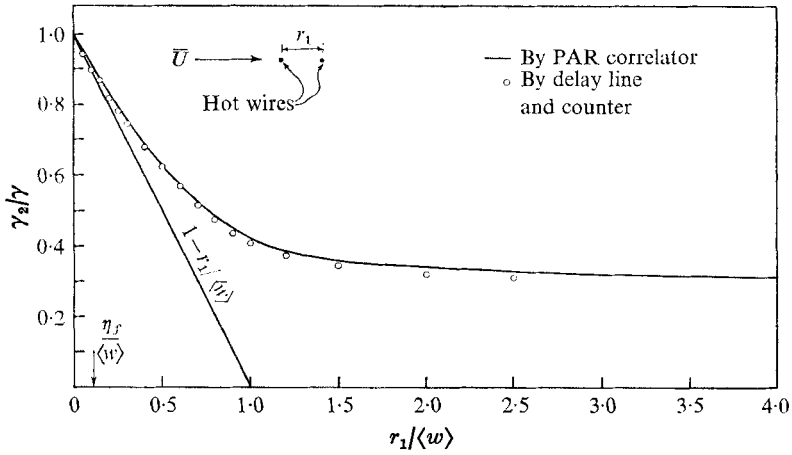

FIGURE 19. Ratio of simultaneous detection intermittency factor to single detection intermittency factor, as a function of equivalent hot-wire probe spacing in downwind direction.

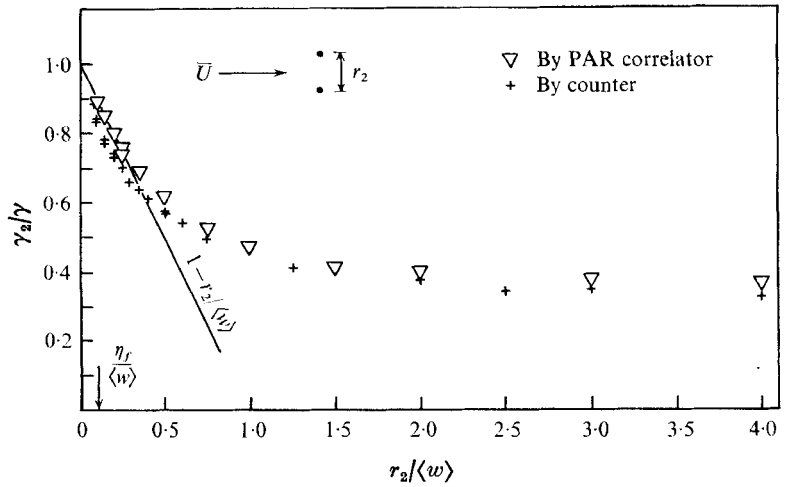

FIGURE 20. Ratio of simultaneous detection intermittency factor to single detection intermittency factor, as a function of hot-wire probe spacing in cross-stream direction. The straight line is the theoretical result for all three geometric models.

Since n (hence m) counts only the entry to (or exit from) fine-structure regions, the average interfacial surface per cubic inch is $4m = 6\,\text{in.}^{-1}$.

The results of the measurements of the coincidence functions are shown in figures 19–22. The dependence of γ_2/γ on $r_1/\langle w\rangle$ and $r_2/\langle w\rangle$ for small values of $r/\langle w\rangle$ agree well with the straight line $\gamma_2/\gamma = 1 - r/\langle w\rangle$, which was estimated for all three types of geometry (table 2). Although this result does not differentiate among the three geometric categories, it is encouraging for our approach, because there are *no adjustable constants*.

The data on $n_2(r_1, 0)/n$ show a quadratic or higher power departure from 1·0, which agrees qualitatively with all three types of geometry. The one elimination appears in $n_2(0, r_2)/n$, see figure 22. From tables 2 and 3 we see that the function

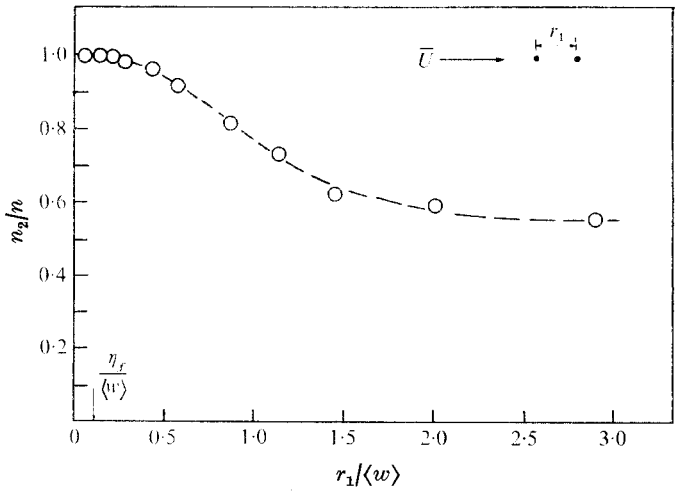

FIGURE 21. Ratio of simultaneous detection event rate to single detection event rate as a function of equivalent hot-wire probe spacing in downwind direction. The dashed line is sketched to follow the data points.

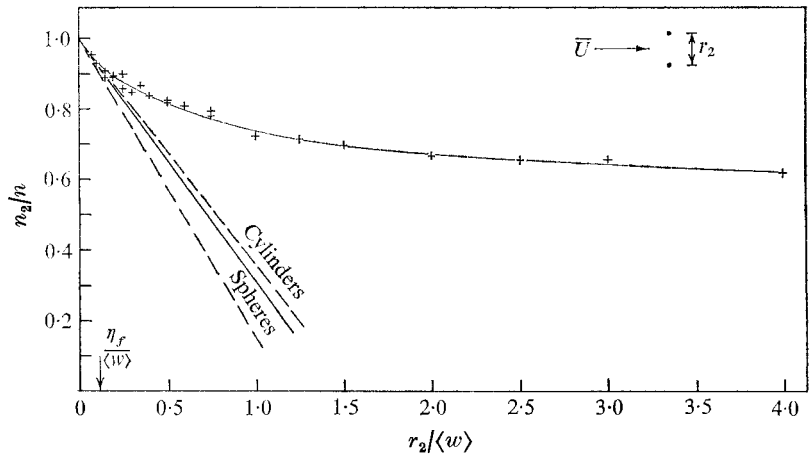

FIGURE 22. Ratio of simultaneous detection event rate to single detection event rate, as a function of hot-wire probe spacing in cross-stream direction. The solid lines are drawn from the data points. The dashed lines are mathematical *upper bounds* for the sphere model and cylinder model corresponding to the lower bounds on α_s and α_c bracketed at equation (5.1).

decreases linearly for sphere and cylinder models, but probably decreases with a higher power of r (hence has zero slope at $r = 0$) for the slab model. In order for the latter to have linear decrease, $g(l)$ would have to have the form

$$g(l) = g(0) + g'(0)l + \ldots, \quad \text{with} \quad g(0) \neq 0 \quad \text{and} \quad g'(0) \neq 0.$$

We therefore make the working conjecture that *the slab category is eliminated.*

Two kinds of numerical checks on the data can be obtained from the values of γ_2/γ and n_2/n at $r = 0$ and of γ_2/γ for $r/\langle w \rangle \to \infty$. In figures 19–22, both γ_2/γ

and $n_2/n \to 1{\cdot}0$ as $r \to 0$, as they must. In figures 20 and 21, we never reach the range $r/\langle w\rangle \gg 1$, but for $r/\langle w\rangle \approx 4$, $\gamma_2/\gamma \approx 0{\cdot}3$ to $0{\cdot}4$. At large separations the signals are independent, so we expect $\gamma_2 \to \gamma^2$, which is roughly satisfied by these measured values.

5. Numerical estimates

In an attempt to find a preference between the sphere and cylinder models, we can make numerical estimates of the coefficients of the corresponding expressions in table 2, for comparison with the data of figures 21 and 22.

We start with $n_2(0, r_2)/n$ because an explicit inequality can be found for the model coefficients. It can be shown that $\langle l^3\rangle\langle l\rangle/\langle l^2\rangle^2$ and $\langle l^2\rangle/\langle l\rangle^2$ are both $\geqslant 1$. Therefore the vertex-tangents for sphere and cylinder models can be written as

$$\left.\begin{aligned}(m_2/m)_s &= 1-\alpha_s r_2/\langle w\rangle \quad (\alpha_s \geqslant 8/3\pi),\\ (m_2/m)_c &= 1-\alpha_c r_2/\langle w\rangle \quad (\alpha_c \geqslant 2/\pi).\end{aligned}\right\} \tag{5.1}$$

The fact that

$$\langle l^2\rangle/\langle l\rangle^2 \geqslant 1 \tag{5.2}$$

is an application of the 'Schwarz inequality' (see, for example, Friedman 1956, p. 454). The other result can be established by writing

$$\begin{aligned}\langle l^3\rangle\langle l\rangle - \langle l^2\rangle^2 &= \frac{1}{A^2}\int_0^\infty l^3 g(l)\,dl \int_0^\infty l' g(l')\,dl' - \frac{1}{A^2}\int_0^\infty l^2 g(l)\,dl \int_0^\infty l'^2 g(l')\,dl'\\ &= \frac{1}{A^2}\int_0^\infty \int_0^\infty (l^3 l' - l^2 l'^2) g(l) g(l')\,dl\,dl'.\end{aligned}$$

In the integrals, l and l' are dummy variables, so we can write

$$\begin{aligned}\langle l^3\rangle\langle l\rangle - \langle l^2\rangle^2 &= \frac{1}{2A^2}\int_0^\infty \int_0^\infty (l^3 l' + l'^3 l - 2l^2 l'^2) g(l) g(l')\,dl\,dl'\\ &= \frac{1}{2A^2}\int_0^\infty \int_0^\infty ll'(l-l')^2 g(l) g(l')\,dl\,dl'.\end{aligned}$$

Since l, l' and g are all $\geqslant 0$, it follows that

$$\langle l^3\rangle\langle l\rangle/\langle l^2\rangle^2 \geqslant 1. \tag{5.3}$$

Figure 22 presents the data on $n_2(0, r_2)/n$, along with the two vertex-tangents corresponding to the lower bounds for α_s and α_c. In order to fit either of these two geometric categories, the data points would have to fall *below* the corresponding line as $r_2/\langle w\rangle \to 0$. *Figure 22 suggests that the sphere model (the 'blobs') may be eliminated.*

A related way of examining the same data is to guess a form for $g(l)$ then compute ranges of α_s and α_c. For convenience, we try

$$g(l) = l^k e^{-bl}, \tag{5.4}$$

which gives

$$\langle l^\rho\rangle = b^{-\rho}(k+\rho)!/k!, \tag{5.5}$$

and

$$\alpha_s \doteq 0{\cdot}85\frac{k+3}{k+2}, \quad \alpha_c \doteq 0{\cdot}64\frac{k+2}{k+1}. \tag{5.6}\dagger$$

† For any $b > 0$.

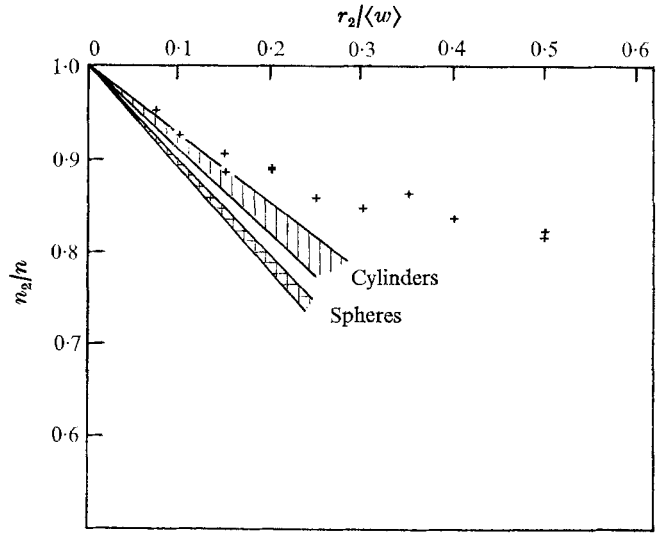

FIGURE 23. Vertex region of figure 22. The shaded areas show ranges of values for sphere and cylinder models, assuming a simple class of functions for size distributions.

Figure 23 shows the ranges covered by (5.1) and (5.6) with $2 \leqslant k \leqslant 10$. Regarded as an empirical fitting attempt, this too favours the cylinder model over the sphere model. The experimental slope corresponds to $\alpha \approx 0{\cdot}7$.

Although we have not established relevant inequalities for the small r_1 coefficients of $n_2(r_1, 0)/n$, we can carry out numerical estimates for the vertex parabolae of the sphere and cylinder models:

$$n_2/n = 1-\beta_s r_1^2/\langle w\rangle^2, \quad n_2/n = 1-\beta_c r_1^2/\langle w\rangle^2, \tag{5.7}$$

with β_s and β_c given in table 2. Using (5.4) again, we find

$$\beta_s \doteq \frac{4}{9}\frac{(k+3)^2}{(k+1)(k+2)}, \quad \beta_c = \frac{3}{8}\frac{(k+1)(k+2)}{k(k+3)}, \tag{5.8}$$

for any $b > 0$. Figure 24 shows the ranges covered by (5.7) and (5.8), with $2 \leqslant k \leqslant 10$. This shows that the cylinder case comes slightly closer to the experiment.

6. Concluding remarks

Our tentative conclusion is that the fluid regions active with turbulent fine-structure are more likely to be rod-like than blob-like or slab-like. We must emphasize the fact that this does not imply straight cylindrical domains all detached from one another. It implies only a tendency to random, slightly 'stringy' structures, which may have quite a few domains of overlap with each other. The dominant geometric trait may even be *ribbon-like*, since a general class of ribbons can be interpreted as rod-like. Another possibility is a mixture of rods and blobs, with a continuous distribution of in-between shapes. Coincidence measurements with three or more probes will be helpful in deciding among these and still more complex alternatives.

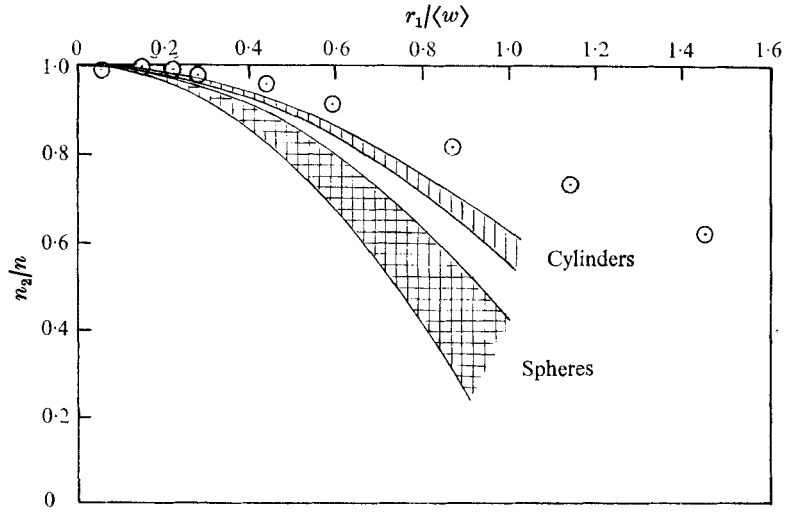

FIGURE 24. Vertex region of figure 21. The shaded areas show ranges of values for sphere and cylinder models, assuming a simple class of functions for size distributions.

To review the picture thus far, we recall from I that the average linear dimension of these fine-structure regions is considerably larger than the turbulent fine-structure therein. At $R_\lambda = 110$, for example, the ratio ranges from 15 to 30, decreasing with decreasing eddy size.

It is interesting to ask whether we can learn anything further from this experiment by geometric study of the spaces between the fine-structure regions. Thinking of the sphere, cylinder and slab models, we expect that the slabs must have interstitial volumes which are blobs, but that the space between widely separated spheres and cylinders ($\gamma \ll 1$) cannot be easily categorized.

If we define intermittency (γ'), occurrence rate (n'), and coincidence functions (γ_2' and n_2') for the inactive regions, these can be computed from the corresponding active region quantities:

$$\gamma' = 1-\gamma, \quad \gamma_2' = 1-2\gamma+\gamma_2, \quad n' = n, \quad n_2' = 2n-n_2, \quad (6.1), (6.2), (6.3), (6.4)$$

$$\langle w'\rangle \equiv \frac{\gamma'\overline{U}}{n'} = \frac{1-\gamma}{\gamma}\langle w\rangle, \tag{6.5}$$

$$\frac{\gamma_2'}{\gamma'} = 1-\frac{\gamma}{1-\gamma}\left[1-\frac{\gamma_2}{\gamma}\right]$$

and

$$n_2'/n' = 2-n_2/n.$$

Since $\gamma' \approx 0{\cdot}7$ for the case studied in detail, no 'rarefied' geometric model can be expected to apply, and we have not pursued this.

This experimental investigation of the statistical geometry of fine-structure regions is only a starting point. More detailed coincidence measurements, with three or more probes, would be interesting. It would also be interesting to detect the geometry in a turbulent shear region, where the rod-like geometry would have a preferred direction.

The fine-scale components of temperature fluctuations have been observed to be intermittent in the wind over the ocean (Gibson, Stegen & Williams 1970). Studies of the statistical geometry of the fine-structure regions of such scalar fields would be worthwhile, as would be efforts to correlate the fine-structure intermittencies of scalar and velocity fields.

Another study of interest would be an attempt to predict the geometry by means of estimates of short-time-average principal strain rates following a fluid element in which fine-structure exists. Betchov (1956) has discussed the dominant signs of the average principal rates in an isotropic turbulent flow. But his results cannot be applied here since he dealt with ensemble averages fixed in space and time, while the average needed here follows a particular fine-structure region.

This work was supported by the U.S. National Science Foundation, under grant GK 10268. It is adapted from part of the Ph.D. thesis of A. Y.-S. Kuo (1970), and was presented at the Annual Meeting of the Division of Fluid Dynamics of the American Physical Society (Kuo & Corrsin 1970). We should like to thank Monica Yoshinaga for her help in clarifying the final sketches.

Appendix

In the two-probe coincidence measurements for the occurrence of the fine-structure, the flow disturbance due to one hot wire prohibits the placement of the second one in its wake. The Taylor approximation†, however, allows us to measure the coincidence functions $\gamma_2(r_1, 0)/\gamma$ and $n_2(r_1, 0)/n$ with a single wire plus a signal delay line. The delayed signal from the hot wire is interpreted as the signal from a fictitious hot wire at a location directly downstream, with separation

$$r_1 = \overline{U}\tau, \tag{A 1}$$

where $\overline{U}$ is the mean velocity and τ is the delay time.

If t_s is the time scale of the fine-structure whose presence we seek, then the approximation is good only for $\tau \ll t_s$. In this investigation of the geometry of fine-structure regions, the fine-structure signal has a spectrum peaked at 3·5 kHz (see figure 19), which corresponds to a wavenumber $k_1 = 17{\cdot}3/\text{cm}$. The eddies of this wavenumber have a characteristic length $1/k_1$ and a characteristic velocity $(k_1 E_{11})^{\frac{1}{2}}$, where $E_{11}(k_1)$ is the one-dimensional energy spectrum. Therefore, a characteristic inertial time scale (essentially the Onsager time scale) is

$$t_s = [k_1^3 E_{11}(k_1)]^{-\frac{1}{2}}, \tag{A 2}$$

which is about 84 ms at $k_1 = 17{\cdot}3/\text{cm}^{-1}$. A more conservative estimate of time scale is the Kolmogorov time scale, actually the order of magnitude of the reciprocal of r.m.s. turbulent strain rate and vorticity:

$$t_K = (\nu/\langle\epsilon\rangle)^{\frac{1}{2}}, \tag{A 3}$$

which is 7·9 ms.

† Demonstrated for a flow much like this one by Comte-Bellot & Corrsin (1971).

As shown in figures 19 and 21, both $\gamma_2(r_1, 0)/\gamma$ and $n_2(r_1, 0)/n$ approach asymptotic values within $r_1/\langle w \rangle \leqslant 4$, which corresponds to $\tau = 1{\cdot}6$ ms, only one-fifth of the smaller time scale, t_K. This comparison of t_K with τ assures that the replacement of two hot wires separated in the mean flow direction by a single hot wire plus its delayed signal is satisfactory, at least for the range $r_1/\langle w \rangle < 1$, where the data are compared with analytical results.

In fact, the signal which was delayed is the on–off binary signal which distinguishes the fine-structure regions from the rest of the fluid. As long as the shape change of the fine-structure domains is small during the time interval τ, the delayed signal is still a good approximation, even if the fine-scale components inside the domains change appreciably. This probably means that $\tau \ll t_s$ is sufficient.

REFERENCES

Batchelor, G. K. 1959 *J. Fluid Mech.* **5**, 113.

Batchelor, G. K. & Townsend, A. A. 1949 *Proc. Roy. Soc.* A **199**, 238.

Batchelor, G. K. & Townsend, A. A. 1956 Turbulent diffusion. *Survey in Mechanics* (ed. G. K. Batchelor and R. M. Davies). Cambridge University Press.

Betchov, R. 1956 *J. Fluid Mech.* **1**, 497.

Comte-Bellot, G. & Corrsin, S. 1966 *J. Fluid Mech.* **25**, 657.

Comte-Bellot, G. & Corrsin, S. 1971 *J. Fluid Mech.* **48**, 273.

Corrsin, S. 1955 *Quart. Appl. Math.* **12**, 404.

Corrsin, S. 1962 *Phys. Fluids*, **5**, 1301.

Corrsin, S. & Phillips, O. M. 1961 *J. Soc. Indust. Appl. Math.* **9**, 395.

Friedman, B. 1956 *Principles and Techniques in Applied Mathematics*, Wiley.

Gibson, C. H., Stegen, G. R. & Williams, R. B. 1970 *J. Fluid Mech.* **41**, 153.

Kuo, A. Y.-S. 1970 Experiments on the internal intermittency in turbulent flow. Ph.D. thesis, The Johns Hopkins University.

Kuo, A. Y.-S. & Corrsin, S. 1970 *Bull. Am. Phys. Soc. Ser.* II, **15**, 1539.

Kuo, A. Y.-S. & Corrsin, S. 1971 *J. Fluid Mech.* **50**, 285.

Lumley, J. L. 1972 *Proc. Convegno sulla Teoria della Turbulenza* (1971), Rome (in press).

Pawula, R. F. 1968 *I.E.E.E. Trans. on Information Theory*, IT **14**, 770.

Tennekes, H. 1968 *Phys. Fluids*, **11**, 669.

Townsend, A. A. 1951*a* *Proc. Roy. Soc.* A **208**, 534.

Townsend, A. A. 1951*b* *Proc. Roy. Soc.* A **209**, 418.

† Strictly speaking, the 'three-dimensional spectrum' and the wavenumber magnitude k are more appropriate here.